ABSTRACT

Title of dissertation: Measuring topology of BECs
in a synthetic dimensions lattice

Dina Genkina
Doctor of Philosophy, 2018

Dissertation directed by: Professor Ian Spielman
Department of Physics

Measuring topology of BECs in a synthetic dimensions lattice

by

Dina Genkina

Dissertation submitted to the Faculty of the Graduate School of the
University of Maryland, College Park in partial fulfillment
of the requirements for the degree of
Doctor of Philosophy
2018

Advisory Committee:
Professor Ian Spielman, Chair/Advisor

Table of Contents

List of Tables

List of Figures

Chapter 2:   Introduction

2.1   Bose-Einstein condensation

2.1.1   Phase transition of a non-interacting Bose gas

Bose gases are characterized by the Bose-Einstein distribution giving the number of atoms $n(E_j)$ occupying each energy eigenstate E_j as

$$n(E_j) = \frac{1}{e^{(E_j - \mu)/k_B T} - 1}, \tag{2.1}$$

where k_B is the Boltzmann constant, T is the temperature in Kelvin, μ is the chemical potential. Assuming the total atom number N is fixed, the chemical potential $\mu(T, N)$ ensures that the total occupation of all $\sum_j n(E_j) = N$.

The Bose distribution leads to Bose-Einstein condensation, the collapse of a macoscopic fraction of the atoms into the ground state. This comes as a direct consequence of the Bose distribution's characteristic -1 in the denominator. Consider the occupation number $n(E_j)$—it must remain positive, as a negative occupation number is unphysical. That means that the quantity $e^{(E_j - \mu)/k_B T}$ must remain greater than 1, or $(E_j - \mu)/k_B T < 0$ for all E_j. Therefore, $\mu \leq E_0$, where E_0 is the ground state energy.

Then, for a given temperature T, there is a maximum occupation number for each excited state given by $n(E_j) = \frac{1}{e^{E_j/k_B T} - 1}$. The only energy state whose occupation number is unbounded is the ground state, as $n(E_0)$ tends toward infinity as μ

tends towards 0. Therefore, as the temperature decreases, the maximum occupation of each excited state decreases until they can no longer support all of the atoms. The remaining atoms then have no choice but to collapse into the lowest energy level and Bose condense.

We will show this quantitatively for the case of a 3-D harmonically trapped gas of atoms, relavant to the experiments described in this thesis. It is convenient to define the fugacity $\zeta = e^{\mu/k_{\mathrm{B}}T}$, and re-write the Bose-Einstein distribution as eigenstate E_j as

$$n(E_j) = \frac{\zeta}{e^{E_j/k_{\mathrm{B}}T} - \zeta}. \tag{2.2}$$

The harmonic oscillator potentail can be written as

$$V(r) = \frac{1}{2}m(\omega_x^2 x^2 + \omega_y^2 y^2 + \omega_z^2 z^2), \tag{2.3}$$

where ω_x, ω_y and ω_z are the angular trapping frequencies along $\mathbf{e}_x$, $\mathbf{e}_y$, and $\mathbf{e}_z$. The eigenenergies with this potential are

$$E(j_x, j_y, j_z) = (\frac{1}{2} + j_x)\hbar\omega_x + (\frac{1}{2} + j_y)\hbar\omega_y + (\frac{1}{2} + j_z)\hbar\omega_z. \tag{2.4}$$

In order to find μ, we must find $\sum_{j_x,j_y,j_z} n(E(j_x, j_y, j_z))$ and set it equal to N. This task is greatly simplified by going to the continuum limit and finding the density of states. To do this, we neglect the zero-point energy (setting $E_0 = 0$, the effects of the zero-point energy are discussed in [?] section 2.5) and assume there is on average one state per volume element $\hbar^3\omega_x\omega_y\omega_z$. Then, the total number of states with energy less than or equal to some value ϵ is given by the volume of a prism made between points $(x, y, z) = (0, 0, 0), (\epsilon, 0, 0), (0, \epsilon, 0)$ and $(0, 0, \epsilon)$ in units of the volume element:

$$G(\epsilon) = \frac{\epsilon^3}{6\hbar^3\omega_x\omega_y\omega_z}. \tag{2.5}$$

The density of states is given by

$$g(\epsilon) = \frac{d}{d\epsilon}G(\epsilon) = \frac{\epsilon^2}{3\hbar^3\omega_x\omega_y\omega_z}. \tag{2.6}$$

Note that the occupation of the ground state is not included in this continuum picture. We can therefore use it only to calculate the total number of atoms in all of the excites states:

$$N_{\text{ex}} = \int_0^\infty d\epsilon\, g(\epsilon)n(\epsilon) = \int_0^\infty d\epsilon \frac{\epsilon^2}{3\hbar\omega_x\omega_y\omega_z}\frac{\zeta}{e^{\epsilon/k_{\text{B}}T}-\zeta} = \frac{(k_{\text{B}}T)^3}{\hbar^3\omega_x\omega_y\omega_z}\text{Li}_3(\zeta), \tag{2.7}$$

where $\text{Li}_3(\zeta)$ is the polylogarithm function[1]. We define the mean trapping frequency $\bar{\omega} = (\omega_x\omega_y\omega_z)^{1/3}$ and the harmonic oscillator energy as $\hbar\bar{\omega}$, with the thermal energy in harmonic oscillator units $\tau = k_{\text{B}}T/\hbar\bar{\omega}$, giving

$$N_{\text{ex}} = \tau^3\text{Li}_3(\zeta). \tag{2.8}$$

Finding the occupation number of the ground state from the Bose-Einstein distribution

$$N_0 = \frac{\zeta}{1-\zeta}, \tag{2.9}$$

we can then find the chemical potential, or equivalently the fugacity ζ, to satisfy

$$N = N_0 + N_{\text{ex}}. \tag{2.10}$$

This is a transcendental equation that can only be solved numerically. We present an example of the solution in Figure 1. Here, we have calculated the fractional population in different harmonic oscillator energy levels for three different temperatures, using trapping frequencies are $\omega_x = \omega_y = \omega_z = 2\pi 50$ Hz, and atom number $N = 10^6$.

---

[1]This calculation was done with Wolfram Alpha, not Russian algebra skills
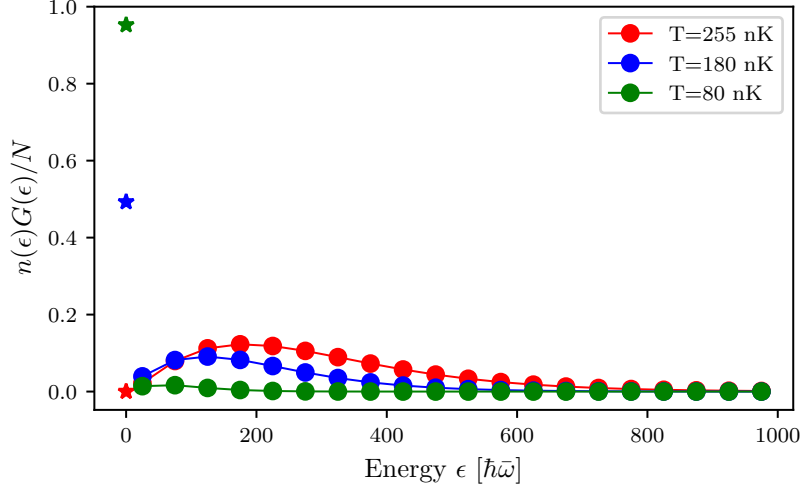
Figure 1: Occupation of energy states of a 3-D harmonic oscillator. The trapping frequencies are $\omega_x = \omega_y = \omega_z = 2\pi 50$ Hz, and the atom number is $N = 10^6$. Dots represent the total fractional population in 50 ajacent energy levels, including degeneracies. The stars represent the fractional population in just the ground state.

For enerigies above the ground state (dots in the figure), we binned 50 energy levels together, such that each dot represents the total fractional population in 50 adjacent levels. This was obtained by integrating eqn. 2.7 from $\epsilon - 25\hbar\bar{\omega}$ to $\epsilon + 25\hbar\bar{\omega}$. The stars represent the fractional population in just the ground state, calculated from eqn. 2.9. Note that at temperature $T = 255$ nK (red), the ground state population is consistent with a continuous extrapolation from the excited state populations and is almost zero. At lower temperatures, $T = 180$ nK (blue) the ground state population is in excess of any reasonable extrapolation from the excited state fractions, and at $T = 80$ nK (green) almost all the atoms are in the ground state.

The onset of Bose-Einstein condensation occurs at a critical temperature T_c. This temperature is defined as the temperature at which the occupation number of excited states is equal to the atom number, ie when the atoms have occupied all available excited states and any remaining atoms will have to pile into the ground state. Since the maximal occupation of the excited states will occur at $\mu = 0$,
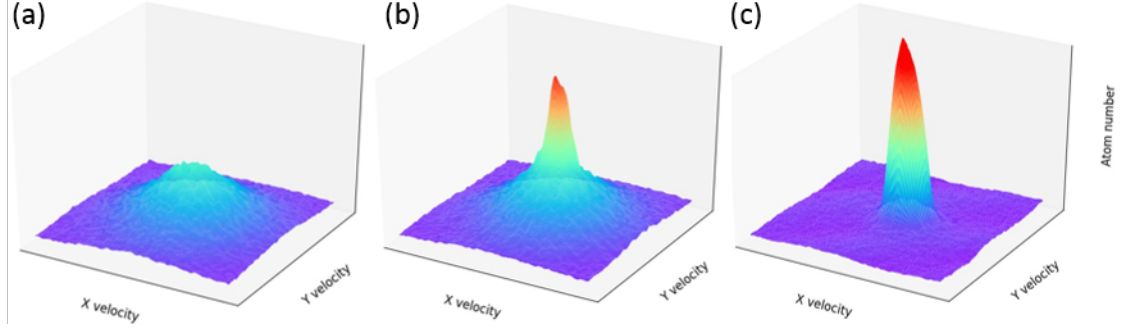
Figure 2: Time-of-flight images of atoms. (a) Above the critical temperature - the atoms are thermally distirbuted. (b) Below the critical temperature - about half of the atoms are condensed in the central peak. (c) Far below the critical temperature - almost all atoms are condensed in the central peak.

the occupation of the excited state is bounded from above by $N_{\text{ex}}(\mu = 0)$, and the critical temperature is defined by

$$N = N_{\text{ex}}(\mu = 0, T = T_c) = \frac{(k_{\text{B}}T_c)^3}{\hbar^3 \omega_x \omega_y \omega_z} Li_3(\zeta = 1). \tag{2.11}$$

Using $Li_3(1) \approx 1.202$, we obtain for a given atom number and trapping frequencies

$$T_c = \frac{1.202N}{k_{\text{B}}^3} \hbar^3 \omega_x \omega_y \omega_z. \tag{2.12}$$

For the parameters in Figure 1, $T_c = 225$ nK.

For temperatures below the critical temperature, the condensation fraction f_c—the fraction of atoms in the ground state—is directly related to the ratio of the temperature to the critical temperature:

$$f_c = 1 - \frac{N}{N_{\text{ex}}} = 1 - \frac{(k_{\text{B}}T)^3}{\hbar^3 \omega_x \omega_y \omega_z} Li_3(\zeta = 1) = 1 - \left(\frac{T}{T_c}\right)^3, \tag{2.13}$$

where in the last step we have plugged in the definition of the critical temperature eqn. 2.12.

Figure 2 shows the progression towards condensation as the temperature of a

cloud of ^{87}Rb is decreased below T_c. The images are obtained via a time-of-flight measurement (see section 3.2.1), where the atoms are allowed to expand freely, mapping the initial momentum to final position, imaged via absorption imaging (see section 3.2). The x and y axes represent momentum along x and y, while the z axis represents the number of atoms. The z axis momentum is integrated over. Figure 2a shows a cloud above the condensation temperature - the momentum distribution is gaussian, given by the Maxwell-Boltzmann distribution. In fig. 2b, the temperature has been decreased below T_c, and about half the atoms have collapsed into the ground state, producing a large peak in atom number around zero momentum. In fig. 2c, the temperature has been decreased even further and almost all the atoms populate the central peak - the distribution is no longer gaussian but a sharp peak around zero momentum.

2.1.2   Interacting Bose gas

In the previous section, we assumed there was no interaction between the atoms other than that enforced by statistics. In this section, we will relax this assumption somewhat and describe the condensed atomic state through its characteristic Gross-Pitaevskii equation.

Since condensation occurs at very low temperatures, and thus very low kinetic energies, we can assume that any scattering processes between the atoms are s-wave and can be described simply by a scattering length a. For ^{87}Rb, relevant to experiments described in this thesis, the scattering length between two atoms in the $F = 2$ hyperfine state is $a = 95.44(7)a_0$ [?], where $a_0 = 5.29 x 10^{-11}$ m is the Bohr radius. The short-range interaction between two particles can be approximated as a contact interaction with an effective strength U_0 as (see [?] section 5.2.1):

$$U(r_1, r_2) = U_0 \delta(r_1 - r_2) = \frac{4\pi\hbar^2 a}{m}\delta(r_1 - r_2), \qquad (2.14)$$

where m is the atomic mass and δ is the Dirac delta function. The full Hamiltonian of the many-body system is then

$$H = \sum_i \frac{p_i}{2m} + V(r_i) + U_0 \sum_{i<j} \delta r_i - r_j, \tag{2.15}$$

where i labels the particles, p_i is the momentum, r_i is the position, and V is the external potential.

We make the mean field approximation by assuming that no interactions between two atoms take them out of the ground state, and hence all atoms can be assumed to be in the same single particle wavefunction, making the overall wavefunction

$$\Psi(r_1, r_2, ...r_N) = \prod_i^N \phi(r_i), \tag{2.16}$$

where ϕ is the single particle wavefunction. It is convenient to define the wavefunction of the condensed state, $\psi(r) = \sqrt{N}\phi(r)$, making the normalization $N = \int dr |\psi(r)|^2$.

The energy of this wavefunction under the Hamiltonian above is given by

$$E = \int dr \left[\frac{\hbar^2}{2m} |\nabla \psi(r)|^2 + V(r)|\psi(r)|^2 + \frac{1}{2}U_0|\psi(r)|^4 \right] \tag{2.17}$$

Given N particles, there are $N(N-1)/2$ unique pairs of particles that can have a pairwise interaction, approximately equal to $N^2/2$ for large N. The N^2 is absorbed into the definition of ψ, but the factor of $1/2$ remains on the final interaction term. The task of finding the condensed eigenstate reduces to minimizing this energy under the normalization constraint $N = \int dr |\psi(r)|^2$. This can be done by using the method of Lagrange multipliers to minimize $E - \mu N$. Then, we can minimize this quantity by finding the point where the derivative with respect to ψ and ψ^* is zero.

Taking the derivative with respect to ψ^* we obtain

$$-\frac{\hbar^2}{2m}\nabla^2\psi(r) + V(r)\psi(r) + U_0|\psi(r)|^2\psi(r) = \mu\psi(r), \qquad (2.18)$$

which is the Gross-Pitaevskii equation. This is a non-linear equation that generally needs to be solved numerically.

There is another approximation that can be made in cases where the atomic density is high enough that the interaction energy is significantly larger than the kinetic energy. Then, the kinetic term in the Hamiltonian can be neglected. This is called the Thomas-Fermi approximation. Then, the wavefunction is given simply by

$$|\psi(r)|^2 = \frac{\mu - V(r)}{U_0}. \qquad (2.19)$$

In this approximation, the probability density simply takes the form of the inverse of the potential. In the case of a harmonically trapped BEC, it is shaped like an inverted parabola. The Thomas-Fermi radius, ie the extent of the particle wavefuntion, is the point where the probability density goes to zero: $\mu - V(r_0) = 0$. For a harmonic trap, along any direction, this is given by $r_0^2 = 2\mu/m\omega^2$.

Figure 3a shows an absorption image of a small fraction of a BEC in situ (see section 3.2.1), meaning as they are in the trap - without expanding in time-of-flight. Therefore, the x and y axis represent position, while color represents the atom number. Figure 3b shows the atom number integrated over the y-axis in blue. The red dashed lines represent a best fit line to a Thomas-Fermi distribution, here an inverse parabola. The black dashed lines represent a best fit of a Gaussian to the atomic distribution. The Thomas-Fermi distirbution matches the atomic distribution more closely in the center where the density is high, but the Gaussian distribution does a better job at the tails of the distribution. This is due to the presence of some thermal atoms, which remain Maxwell-Boltzmann distributed.

(a)

(b)
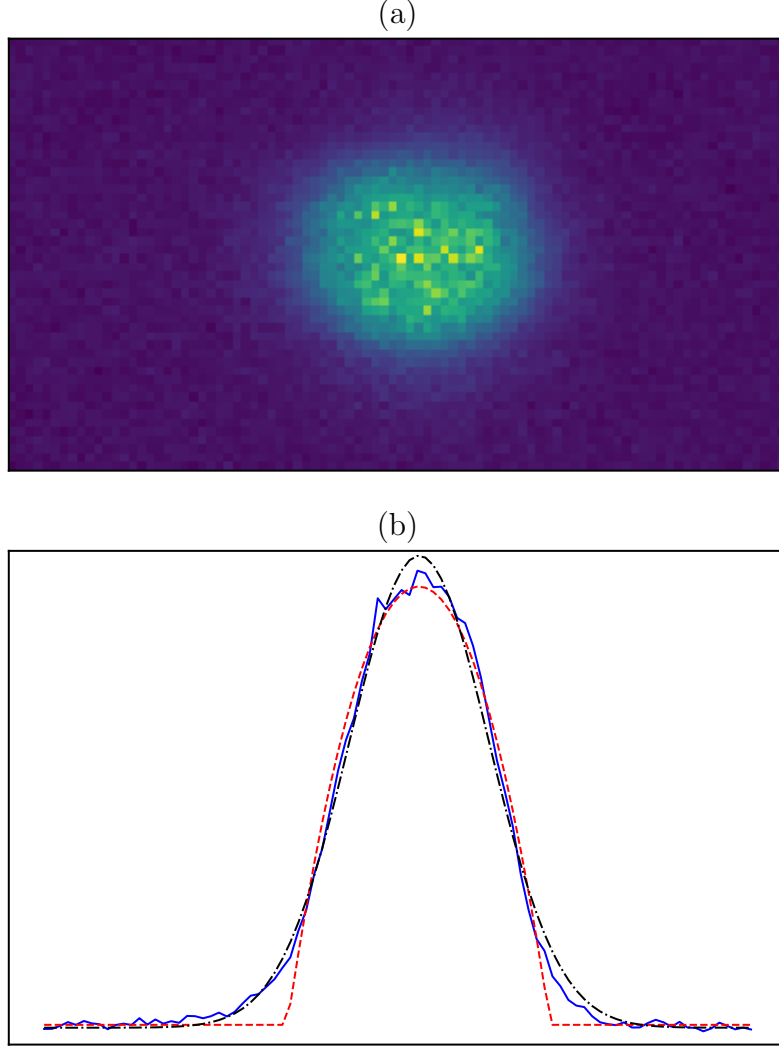
Figure 3: In situ measurement of a fraction of bose condensed atoms. (a) Absorption image taken of $\approx 1\%$ of the cloud. The x and y axes represent x and y position, while color represents the atom number. (b) The blue line repesents atom number as a function of position along hte x axis, integrated over the y axis. The black dashed line represents the best fit of a Gaussian function to the atomic distribution. The dashed red line represents the best fit of a Thomas-Fermi profile to the atomic distribution.

2.2 Degenerate Fermi Gas

2.2.1 Fermi statistcs and the onset of degeneracy

The occupation of different energy levels by Fermions is given by the Fermi-Dirac distribution:

$$n(\epsilon) = \frac{1}{e^{(\epsilon-\mu)/k_B T} + 1}. \tag{2.20}$$

The difference from the Bose-Einstein distribution is simply the sign of the 1 in the denominator. This has important implications, however. First, since e^x varies between 0 and inf, the occupation $n(\epsilon)$ varies between 1 and 0 - a consequence of the Pauli exclusion principle. Second, as the temperature T tends towards 0, there become two distinct cases: $\epsilon - \mu > 0$ and $\epsilon - \mu < 0$. If $\epsilon - \mu > 0$, $e^{(\epsilon-\mu)/k_B T}$ tends towards inf, and $n(\epsilon)$ tends towards 0. If $\epsilon - \mu < 0$, $e^{(\epsilon-\mu)/k_B T}$ tends towards 0, and $n(\epsilon)$ tends towards 1. Therefore, at $T = 0$, the energy states below the chemical potential μ are maximally occupied (with probability 1) and the energy states above the chemical potential are unoccupied.

We can use this to determine the chemical potential at $T = 0$ by constraining the total atom number:

$$N = \sum_j n(E_j) = \sum_{\epsilon_j < \mu} 1. \tag{2.21}$$

Again, we take the common example of the 3-D harmonic trap. Then the task reduces to simply finding the number of energy levels at or below a certain energy μ. This is given by eqn. 2.5. From this, we find the chemical potential at zero energy, which is known as the Fermi energy E_F, as

$$E_F = (6N)^{1/3}\hbar\bar{\omega}, \tag{2.22}$$

where $\bar{\omega} = (\omega_x \omega_y \omega_z)^{1/3}$ is the geometric mean of the three trapping frequencies.

From the Fermi energy, we can define the associated Fermi temperature T_F as

$$T_F = \frac{(6N)^{1/3}\hbar\bar{\omega}}{k_B},$$

(2.23)

and the Fermi momentum $\hbar k_F$ as

$$\hbar k_F = \sqrt{2mE_F},$$

(2.24)

where m is the mass of the Fermion.

For higher temeperatures, we can solve for the chemical potential, or the fugacity ζ, by integrating the Fermi-Dirac distribution weighted by the density of states (eqn. 2.6) to obtain

$$N = \int_0^\infty \frac{\epsilon^2}{2\hbar^3\bar{\omega}^3} \frac{\zeta}{e^{\epsilon/k_B T} + \zeta} = -\frac{(k_B T)^3}{\hbar^3\bar{\omega}^3} Li_3(-\zeta),$$

(2.25)

where Li_3 is again the polylogarithm function. Again, this is a transcendental equation that can be solved numerically. However, in contrast to the BEC case, we do not have to consider the ground state occupation separately, as it is bounded by 1 like every other state.

We show an example of the occupation distribution for different temperatures in Figure 4. Here, we have used the same parameter values as for the BEC case: $N = 10^6$ and $\omega_x = \omega_y = \omega_z = 2\pi 50$ Hz. The Fermi temperature for these parameters is $T_F = 436$ nK. For illustrative purposes, we plot $n(\epsilon)$, unweighted by the density of states $g(\epsilon)$. At zero temperature (red line in the figure), only states below the Fermi energy are occupied. At higher temperatures, the distribution is smoothed out (green and orange lines) until at the Fermi temperature there is almost no significance to the Fermi energy.

In contrast with Bose-Einstein condensation, the transition to a Degenerate
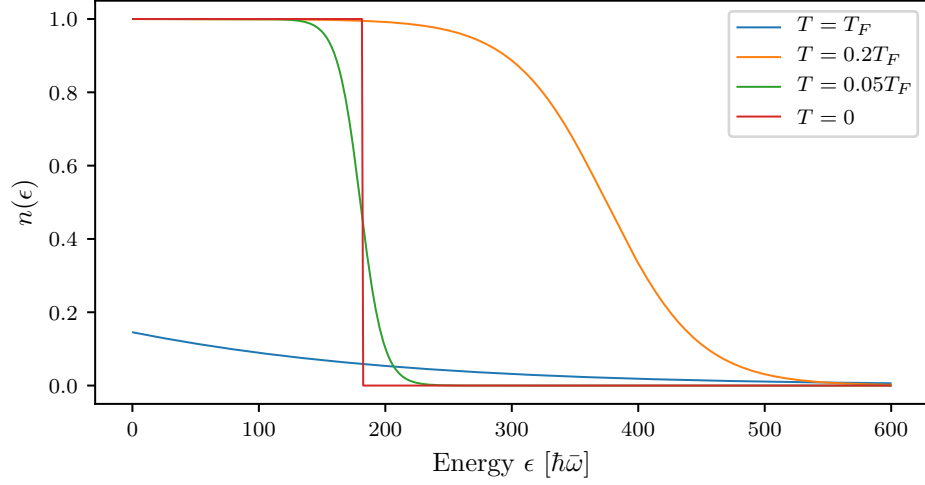
Figure 4: Occupation number as a function of energy for a Fermi gas of $N = 10^6$ atoms in a 3-D harmonic oscillator with frequencies $\omega_x = \omega_y = \omega_z = 2\pi 50$ Hz. The Fermi temperature for these parameters is $T_F = 436$ nK.

Fermi Gas (DFG) is not a phase transition, and there is no absolute measure of the onset of degeneracy. Instead, a Fermi gas can be considered degenerate when the occupation function $n(\epsilon)$ differs significantly from that of a thermal gas. This occurs when the temperature is of order $0.2T_F$.

2.2.2   Interactions and Feshbach resonances

Although the magnitgude of the contact interaction U_0 for DFGs is not intrinsially different from that of BECs. There are, however, two key differences. First, the Pauli exclusion principle forbids s-wave interactions between atoms of the same spin. Higher partial wave interactions are 'frozen out' at low temperatures, when the impact parameter of the collision becomes larger than the effective cross section of interactions (see [1], sec. 2.1.2). Therefore, in order to observe interactions, and indeed to cool the gas to degeneracy, another species needs to be present so that intraspecies s-wave interactions can occur. This can be a different atomic species or a different spin state of the same atom.

Second, the densities of standard DFGs ($\approx 10^{12}$ atoms/cm³) are much lower than that of BECs ($\approx 10^{14}$ atoms/cm³). Since the likelyhood of two-body collisions is proportional to the atomic density ρ^2, this leads to a much smaller effect of interactions in DFGs.

A widely used technique for enhancing interaction effects in DFGs is Feshbach resonances. A Feshbach resonance occurs between two spiecies (either atomic species or spin species of the same atom) when the open channel, ie the two particles independently in their external potential, energetically approaches a closed channel, ie a bound molecular state of the two species, shown schematically in Figure 5a.

Generally, the atoms in an open channel are energetically sensitive to a bachground magnetic field B via the hyperfine interaction $H_B = \mu \cdot B$, where μ is the magnetic dipole moment. Tuning the magnetic field should therefore tune the energy of the open channel. The molecular bound state may also have an overall magnetic moment, but it is generally not identical to that of the two atoms in the open channel, and therefore varies differently with the background field. Figure 5b shows an example where the bound state has zero magnetic moment. Here, the energy of both the closed and open channel as a function of backround magnetic field B is plotted in the vicinity of a Feshbach resonance. The resonance occures at a field B_0 where the energies of the two channels coincide.

Assuming there is at least infinitesmal coupling between the closed and open channels, as the energies of the two channels approach each other the perturbative correction term to the energy grows and the interaction between the atoms is effected. This is most easily seen in the s-wave case through changes the scattering length a. In the case where there are no inelastic two-body channels, such as for the ^{40}K resonance discussed in this thesis, the interatomic scattering length as a
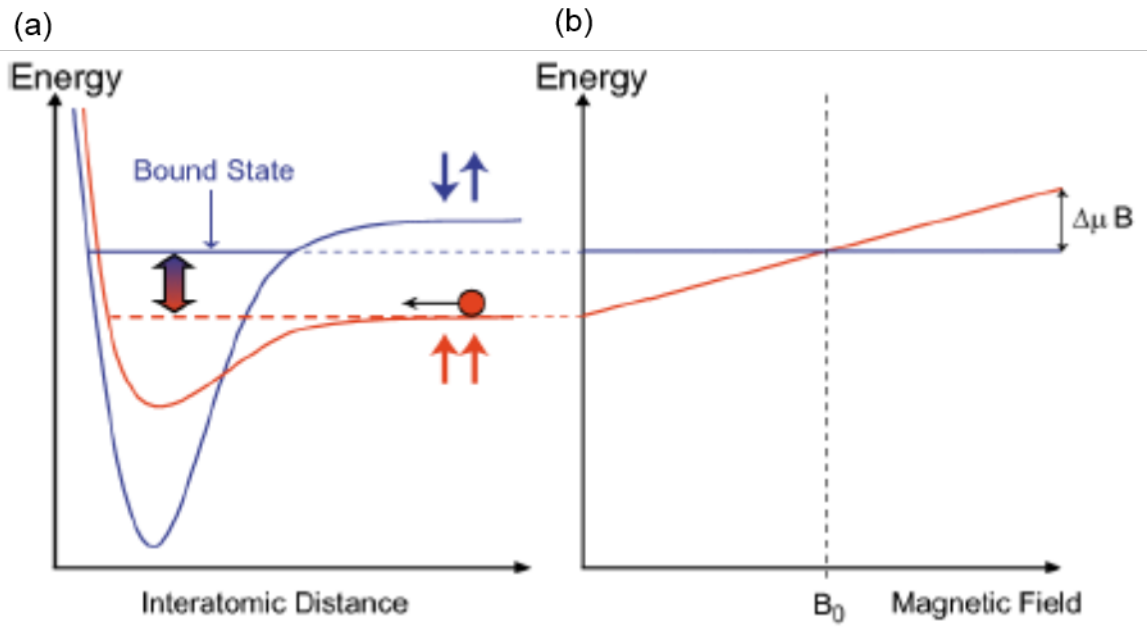
Figure 5: Schematic of a Feshbach resonance. (a) Pictoral representation of energy as a function of interatomic distance for an open channel (red) and closed channel (blue). (b) Energy as a function of background magnetic field B for the closed (blue) and open (red) channels. The energies coincide at the Feshbach resonance point B_0. Energy of Figure taken from [1].

function of background field is given by [21]

$$a(B) = a_{\mathrm{bg}} \left(1 - \frac{\Delta}{B - B_0} \right), \qquad (2.26)$$

where a_{bg} is the background scattering length, Δ is the width of the resonance, and B_0 is the field value at which the resonance occurs. The scattering length diverges at the resonance.

The tunability of interactions provided by Feshbach resonances has allowed for creation of molecular Bose-Einstein condensates from Fermi gases [?,?,?] as well as observation of the phase transition from the Bardeen-Cooper-Schrieffer (BCS) superconduting regime to the BEC regime at sufficiently low temperatures [?,?,?,11].

2.3   RbK apparatus

The rubidium-potassium (RbK) appartus at NIST Gaithersburg has been previously detailed in [?,?,7]. In this thesis, we will give a brief overview of the apparatus and how it is used to produce BECs of ^{87}Rb and DFGs of ^{40}K, and only give detailed documentation for those parts of the apparatus that differ from previous works.

A photograph of the main experiment is shown in Figure 6. This is mounted on an optical table, with the science chamber elevated above the surface of the table. The atoms start at the ovens (off to the right, not in the photograph) and travel down the Zeeman slower until they are trapped in the science chamber. The optical dipole trap laser, as well as the 1-D optical lattice laser, are located on the optical table and coupled into optical fibers, which are output on the main floor of breadboard before being sent towards the atoms. All other lasers are located on other optical table and brought over to the experiment table via optical fibers.

Figure 7 details the beam paths of the light going through the atoms. Figure
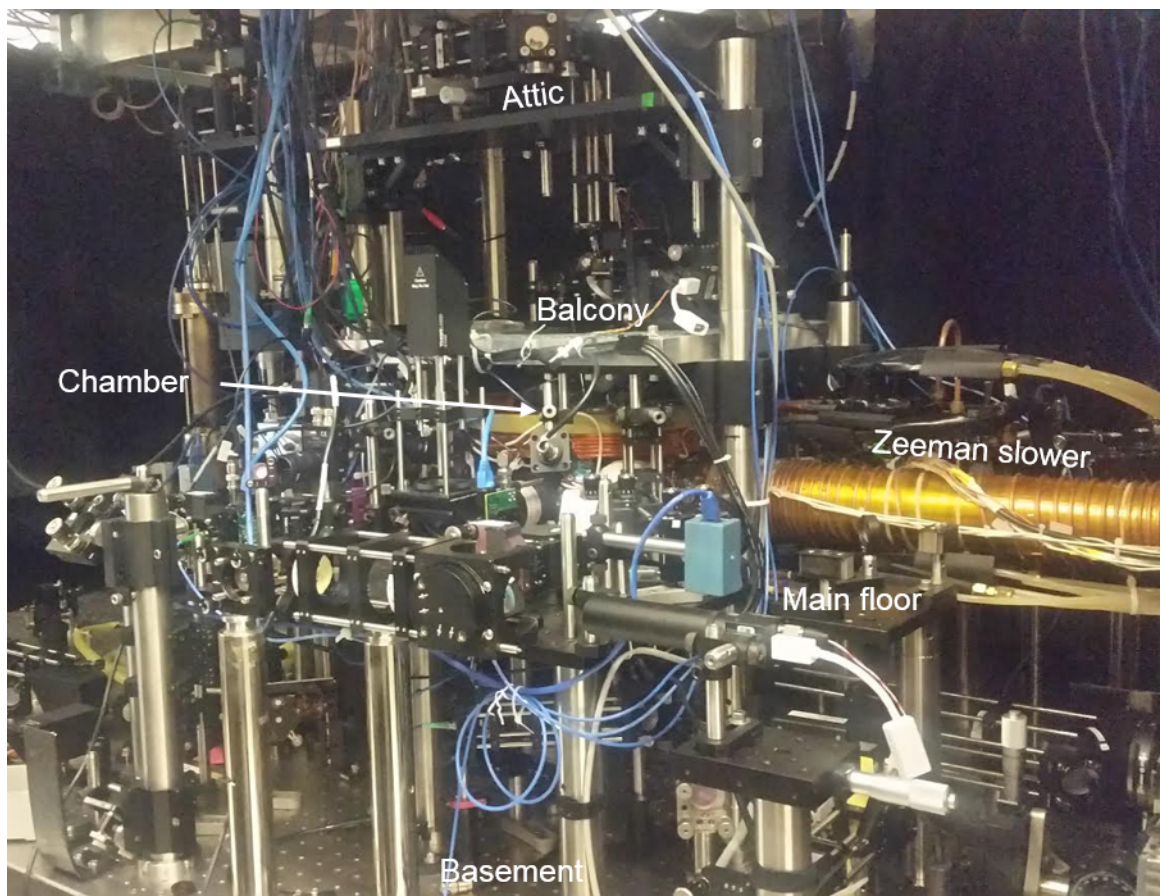
Figure 6: Photograph of RbK apparatus at NIST Gaithersburg. The main science chamber is at the center, hidden behind optics and coils. The Zeeman slower connects the atomic ovens (not shown) to the chamber. There are several levels of breadboards on which optics are mounted, labelled here as basement (surface of optical table), main floor, balcony and attic.

7a shows a side view of the apparatus. The up and down going MOTcooling beams are shown in red, reaching the atoms when the flipper mirrors M_{top} and M_{bottom} are flipped in. The down going probe beam, used for imaging along the $x - y$ axis both in situ and in time-of-flight, is shown in solid blue. The probe beam is split via a polarizing beam splitter cube to allow for both in situ and time-of-flight imagnig of the same cloud, shown in the inset in fig. 7b and described in greater detail in sec. 2.3.2. The dashed blue line represents the upward going probe beam introduced for alignment purposes, described in greater detail in sec. 2.3.2.

Figure 7b show's a bird's eye view of the apparatus, with optics on the main floor breadboard. The slower cooling (solid dark blue) and slower repump (dashed dark blue) are coming in from the left to slow the atoms as they are moving through the Zeeman slower. The remaining four MOT cooling beams, coming from four opposing directions, are shown in red. They reach the atoms when their flipper mirrrors, $M1 - 4$, are flipped in. All six flipper mirrors are computer controlled by the same digital channel, so they can be flipped in and out together. Only the beams going in through mirrors $M1$ and $M2$ are accompanied by MOT repump light, dashed red lines. The optical dipole trap beams (solid green) come from the same 1064 nm laser (IPG YDL-30-LP), and are split via an acousto-optic modulator into two orders, which enter from opposite directions and intersect each other at approximately a 90 degree angle, providing confinement along all three axes. There are three available Raman beams (solid magenta): Raman A, entering past the flipped-out $M2$ mirror, Raman B, at 90 degrees to Raman A entering past the $M1$ mirror, and Raman C, counter-propagating with Raman A and entering past the $M4$ mirror. There is a 1-D optical lattice beam (dashed green), also 1064 nm (IPG YAR-10K-1064-LP-SF, seeded by a pick off from a), sent in past the $M2$ mirror and retroreflected on the opposite end of the chamber to form a standing wave patter. Lastly, there is another imaging beam, imaging the atoms along the $x - z$ plane,

going to a Flea3 camera.

Figure: coils

2.3.1 Procedure for making a BEC

Brief description of BEC making procedure

In the first step of the BEC making procedure, the atoms starting at the oven are cooled via a Zeeman slower and captured in a Magneto-Optical trap in the sicence chamber. During this step, the Zeeman slower is on, with both the coils and the slower cooling and repump lights on. These beams (dark blue in Figure 7b)address the $F = 2$ to $F = 3$ transition of ^{87}Rb. At the same time, the flipper mirrors $M1-4$,M_{bottom},M_{top} are flipped in and the MOT cooling and repump beams (red in Figure 7) are on. The quad coils are on in anti-Helmholtz configuration with 25 A of current running through them, producing a field gradient of $\frac{dB_z}{dz} \approx 13$ Gauss/cm. This step can be set to take anywhere from ≈ 0.7 s to ≈ 5 s depending on how many atoms are necessary.

Next is the optical molasses step. For this step, the Zeeman coils and slower lights are turned off. The quad coil current is also switched off, leaving just the MOT cooling light and only leakage MOT repump light. [LOOK UP MOLASSES DETUNINGS EXACTLY]. This is the sub-doppler cooling stage. Since the repump light is all but off in this step, the atoms are also depumped into the $F = 1$ manifold. Then, the atoms are optically pumped into the $|F = 1, m_F = -1\rangle$ state to make them trappable by the quadropole field. This is done by turning on the slower repump beam (dashed dark blue in fig. 7b) [LOOK UP TIME]. Then, the XZ imaging beam (blue in fig. 7b) is briefly turned on to get rid of any remaining $F = 2$ atoms.

Next, we compress the atoms and perform forced Rf evaporation. To compress, the quad coils arefirst turned on to 130 A. After holding for 20 ms, we sweep the

(a)

Attic

alignment
Flea3

Balcony M_{top}

Main floor

e_z, e_x, e_y

M_{bottom}

Basement — inset

(b)

-1st order 0th order

e_y, e_x, e_z

M3 M4

Zeeman slower

M2 M1

A B

XY
in situ
Flea3

XY TOF
PIXIS

XZ Flea3 inset

Main floor

→ MOT cooling beams	◣ Mirror
⇢ MOT repump beams	in/out Flipper mirror
→ Slower cooling beam	□ Acousto-optic modulator
⇢ Slower repump beam	Optical fiber
→ Optical dipole trap beams	◁ Camera
⇢ 1-D Lattice beams	◨ PBS cube
→ Raman beams	▬ Quarter waveplate
→ Imaging beams	
⇢ Alignment imaging beam	

Figure 7: Schematic of RbK apparatus. (a) Side view of apparatus. Only beams propagating along the e_z direction through the atoms is pictured. (b) Top view of apparatus. Only beams propagating along the $x - y$ plane are shown. Schematic is not to scale and the angles are approximate

current linearly to 250 A in 200 ms. The forced rf evaporation is then performed by turning on the rf coupling field and sweeping the frequency from 20 MHz to 4 MHz in 4 s [CHECK TIME] to couple the highest energy atoms from $|F = 1, m_F = -1\rangle$ to $|F = 1, m_F = 0\rangle$ and allow them to escape the trap. The slow ramp is designed to allow the system to rethermalize through collisions as the hottest atoms are ejected. During rf evaporation, the crossed optical dipole trap

Then, the atoms are loaded into the crossed optical dipole trap, where further evaporation occurs.

The lack of repump caused the atoms to be optically pumped into the F = 1 ground state. Whe optically pumped the atoms into the —F = 1,mF = 1i for 1 ms state by illuminating them with the slower repumping light. We then turn on the xz imaging probe to blow away any remaining F = 2 atoms. We then rapidly turned on a quadrupole magnetic trap with a current of 130 A in our large coils in an anti-Helmholtz configuration. After a 20 ms hold, we linearly ramped the current from 130 A to 250 A in 0.2 s to compress the atoms and increase their collision rate. After compression, we turn on our optical dipole trap. For all experiments in this thesis, the beam propagating along ex has the smallest beam waist (See Tab. 4.4 for specific beam waist information) in ez, the direction of gravity. We turned on the dipole trap with most of the power in this beam and at the highest power possible. We turned on our rf magnetic field and linearly ramped the frequency from 22 MHz to 4 MHz in 4 s. This flipped the spin of the highest energy atoms and then allowed the remaining atoms to thermalize at a lower temperature. We decompressed the quadrupole trap by ramping the current in the coils from 250 A to 60 A in an exponential ramp with time constant = 1.5 s over 3 s. While decompressing, we lowered the atoms into the dipole trap by ramping a smaller bias coil in Helmholtz configuration providing field in ez from 10 A to 8 A. This lowers the quadrupole zero toward the dipole trap. We completed the evaporation to BEC in the optical

dipole trap. The quadrupole is still on, just barely compensating for gravity. We evaporated in the optical dipole trap in either 3 s for typical BECs or 5 s for an elongated BEC. For the overall power in the dipole trap, we either used a linear ramp or sometimes we used an OHara ramp [103] to ramp from the initial power command to the final power command. The OHara ramp ramps the dipole potential more rapidly at first, then slows down. Also during this evaporation we linearly ramped the amplitude command to acousto-optic modulator (AOM) controlling the power balance in the two beams of our dipole trap. This further lowered the power in the beam along ex while increasing the power in the ey beam. After evaporation in the dipole trap, we ramped the quad current to 0 A with an exponential ramp with time constant $= 0.8$ s over 5 s. Ramping off the quadrupole continued the evaporation by decreasing the optical trap depth due gravity. This sequence creates a —F = 1,mF = 1i 87Rb BEC in an optical dipole trap.

2.3.2   Changes to apparatus for Rubidium

Differences from Lauren's thesis:

Put master laser setup in PBS cube on XY imaging system Describe Hsin-I's new imaging path Describe extra lens for beam shaping the dipole trap

2.3.3   Procedure for making a DFG

Brief description of DFG making procedure (of old) Our Zeeman slower slowed both 87Rb and 40K atomic beams. Because 40K is lighter than 87Rb, the atoms will bloom or acquire a transverse velocity at the output of the slower. To increase the number of 40K atoms ultimately captured in the MOT, we cooled the atoms in an orthogonal direction to the slower immediately after the oven, but before the slower. We loaded the 40K MOT first by turning on the slower cooling, slower repump, transverse cooling, MOT cooling, and MOT repump light for 40K, but

not 87Rb. After 7 s of 40K MOT loading, we also loaded 87Rb for a 1.5 s of MOT loading. The current in the large, anti- Helmholtz was 25 A, similar to BEC creation. We cooled both species in optical molasses for 2 ms. For 87Rb, we did an abbreviated ramp of the MOT cooling light detuning from 33 MHz to 53 MHz away from resonance. For 40K, we lowered the intensity of the MOT cooling light without modifying its detuning. We optically pumped both species into their maximally stretched magnetically trappable states, —F = 9/2,mF = 9/2i for 40K and —F = 2,mF = 2i for 87Rb. 40K had a dedicated optical pumping beam. We used the slower rempump and MOT repump light, as well. For 87Rb, we pulsed on the slower light and both the slower and MOT repump light. Both species were then loaded into a quadrupole magnetic trap with a current of 130 A in our large coils in anti-Helmholtz configuration. The currents in our 3 pairs of Helmholtz bias coils are listed in Tab. 4.2 for both the creation of a DFG and a BEC. Similar to the BEC sequence, we compressed the magnetic trap by linearly ramping the current in in the large coils from 130 A to 160 A. After compression, we cooled our atoms evaporatively via forced rf evaporation, sweeping the rf frequency from 18 MHz to 2 MHz in 10 s. During evaporation, the magnetic trap was plugged by a = 532 nm beam, tightly focused to 30 m and 5W in power, providing a repulsive potential around the quadrupole zero to prevent Majorana losses. Since the 40K atoms were spin polarized and therefore only interacted by increasingly suppressed p-wave interactions, they re-thermalized largely due to sympathetic cooling with 87Rb atoms. After the 10 s evaporation in the plugged quadrupole trap, we turned on our crossed beam optical dipole trap at full power (6W) predominantly in the more tightly focused beam. Both the green plug beam and the optical dipole trap remain on as we decompressed the quadrupole trap by exponentially ramping the current from 160 A to 25.5 A with time constant = 1.5 s over 3 s. Next, we evaporated in the optical dipole trap by ramping the relative power balance in the

crossed beams to their final balance in 3 s. This reduced the overall dipole trap depth because more power was in a beam with a larger beam waist. We also ramped off the power in the green plug beam during this 3 s as well. We simultaneously evaporated from the dipole trap by lowering the overall optical power with an OHara ramp and using an exponential ramp to turn off the quadrupole field with time constant $=$ 1.5 s over 2 s. At this juncture, we had $|F = 2, m_F = 2\rangle$ 87Rb atoms and $|F = 9/2, m_F = 9/2\rangle$ 40K atoms in our crossed beam optical dipole trap. We then used adiabatic rapid passage (ARP) to transfer the 87Rb atoms from the $|F = 2, m_F = 2\rangle$ state to the $|F = 1, m_F = +1\rangle$ ground state via 6.8556 GHz microwave coupling (20.02 MHz from the zero field resonance) followed by ramping the current in the bias ez coils 1 A in 50 ms. This state was chosen to minimize spin changing collisions with 40K atoms during further evaporation [22]. After the ARP, we briefly applied an on-resonant probe laser, ejecting any remaining 87Rb atoms in the F $=$ 2 manifold from the trap. We evaporated further in the optical trap again using an OHara ramp for 1 s. The optical potential from the dipole trap no longer holds the 87Rb against gravity. We used a second ARP to transfer the 40K atoms into the $|F = 9/2, m_F = 9/2\rangle$ state by illuminating the atoms with a 3.3 MHz rf field and sweeping the current in the bias ez coils 5 A in 150 ms. At the end of this sequence, we had a DFG of about 75, 000 40K atoms in the $|F = 9/2, m_F = 9/2\rangle$ state with temperature $0.4 T_F$.

2.3.4 Current status of Potassium apparatus

Differences from Lauren's thesis: Describe 2D MOT'

Chapter 3:   Atom Light Interactions

3.1   Near-resonant atom-light interaction

In this section, we will assume the atom can be treated as a two-level system: one with a ground and excited atomic state, with an energy difference of energy difference $\hbar\omega_0$. When such an atom, starting in the ground state, is illuminated by a laser beam with frequency $\hbar\omega_{\mathrm{L}}$, there are three kinds of transitions that occur: during aborption the atom aborbs a photon from the laser and goes from the ground to the excited state; during stimulated emission, the atom emits a photon into the field of the laser beam and jump from the excited to the ground state; during spontaneous emission, the atom decays to the ground state from the excited state with no help from the laser, emitting into a random vacuum mode. Stimulated emission results in coherent light co-propagating with the laser beam, while spontaneous emission results in light scattering incoherently in any direction. The rate of spontaneous emission from an excited state is given by the natural transition linewidth of the transition Γ.

On timescales short compared to $1/\Gamma$, spontaneous emission can be ignored, and an atom undergoes coherent Rabi oscillations between the ground and excited states via cycles of absorption and stimulated emission [4]. Taking c_g and c_e to be the time-dependent coefficients multiplying the eigenstate wavefuntions of the ground and excited state respectively, and assuming the atom starts in the ground

state $c_g(t = 0) = 1$, the excited state population is given by

$$c_e(t) = -i\frac{\Omega}{\Omega'}\sin\left(\frac{\Omega't}{2}\right)e^{-i\delta t/2}, \qquad (3.1)$$

where Ω is the Rabi frequency given by $\Omega^2 = \frac{\Gamma\lambda_L^3}{h(2\pi)^3}I$, with λ_L as the laser wavelength, h as Plank's constant and I as the laser intensity, $\Omega' = \sqrt{\Omega^2 + \delta^2}$ is the generalized Rabi frequency and $\delta = \omega_0 - \omega_L$ is the detuniong of the laser from atomic resonance.

In the regime where spontaneous emission cannot be ignored, Rabi oscillations of each individual atom are intermittently interrupted by decay to the ground state. Averaging over an atomic ensamble, on the time scale of a single Rabi oscillation the overall excited state population reaches a steady state, and the rate of spontaneous emission becomes constant. Since during spontaneous emission the ejected photon can go into any vacuum mode, this process can be thought of as the scattering of photons by the atoms. This scattering rate is given by [4]

$$\gamma_{\text{sc}} = \frac{\Gamma}{2}\frac{I/I_{\text{sat}}}{1 + 4(\delta/\Gamma)^2 + I/I_{\text{sat}}}, \qquad (3.2)$$

where I_{sat} is the saturation intensity. This is the intensity at which the timescale of spontaneous emission matches the Rabi oscillation rate, reducing the capacity for absorption of extra light.

3.2 Absorption imaging

Absorption imaging takes advantage of the on-resonant interaction described in the previous section. An on or near-resonant laser beam ($\delta/\Gamma \ll 1$) is shined at the atoms, and the aborbed light acts to create a shadow in the shape of the atoms in the laser beam. This beam with the shadow is then imaged on a camera, in our case a CCD, as depicted in Figure 1a (top). This is called the atom image,
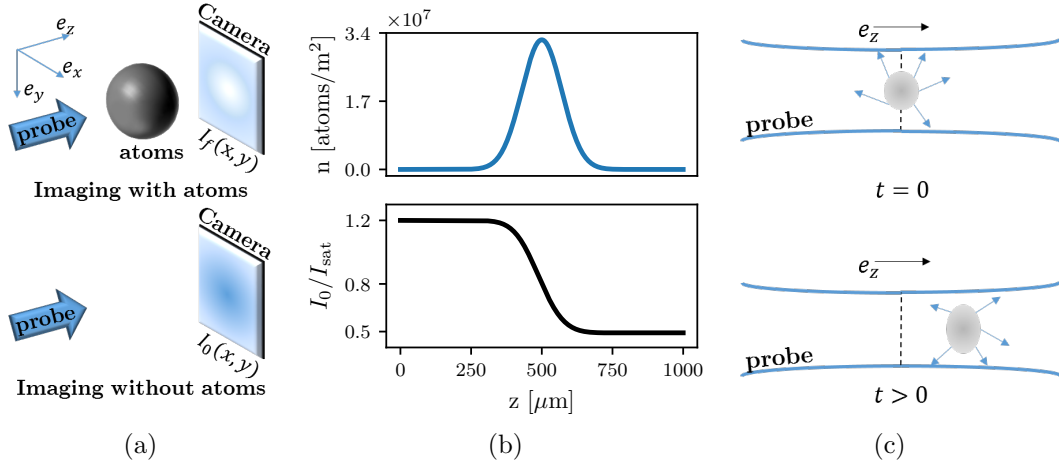
Figure 1: Absorption imaging. (a) Near resonant probe light illuminates the atoms, and the transmitted light (containing a shadow of the atoms) is imaged on the camera. A second image taken with no atoms provides a reference. (b) The probe beam is partially absorbed as it traverses the cloud, and the intensity seen by atoms further along the imaging direction $e_{\mathbf{z}}$ is lowered. (c) An atomic cloud illuminated by a probe light field absorbs photons from the probe and re-emits them in all directions. This process results in a net acceleration of the cloud in the direction of the probe light as well as diffusive spreading in the transverse directions.

and the intensity distribution over the camera is denoted by $I_f(x, y)$, where the subscript f stands for final - the intensity after the light has encountered the atoms. To quantify the 'shadowed out' intensity, after the atoms have left the trap the same laser intensity is shined directly at the camera, as in Figure 1a (bottom). This is called the probe image, and the intensity distribution over the camera is denoted by $I_0(x, y)$, where the subscript 0 indicated initial - the intensity before the light had encountered the atoms.

To recover the atom number distribution encountered by the light, consider an atomic cloud with 3D density $\rho(x, y, z)$. Since we can only obtain 2D information from the camera, we can only hope to recover a 2D atomic column density $n(x, y) = \int \rho(x, y, z)\mathrm{d}z$. Focusing in on a single pixel of the camera, we can consider a single value of I_0 and I_f to recover a local n. As the laser light propagates through the atomic cloud, the intensity of the light will diminish due to absorption. This

absorption as a function of propagation direction z can be expressed using the scattering rate equation Eq. 3.2 as the number of photons scattered by the atoms (proportional to the atomic density times the scattering rate) times the photon energy $\hbar\omega_{\mathrm{L}}$:

$$\frac{d}{dz}\frac{I(z)}{I_{\mathrm{sat}}} = -\hbar\omega_{\mathrm{L}}\rho(z)\gamma_{sc}(z) = -\rho(z)\sigma_0 \frac{I(z)/I_{\mathrm{sat}}}{1 + 4\delta^2/\Gamma^2 + I(z)/I_{\mathrm{sat}}}, \qquad (3.3)$$

where the resonant scattering cross section is $\sigma_0 = 3\lambda_0^2/2\pi$, and λ_0 is the wavelength asociatted with atomic resonance.

Integrating both sides of Eq. 3.3, we obtain

$$\sigma_0 n = \left(1 + 4\delta^2/\Gamma^2\right)\ln(I_0/I_f) + \left(I_0 - I_f\right)/I_{\mathrm{sat}}. \qquad (3.4)$$

The quantity $OD = ln(I_0/I_f)$ is called the optical depth of the cloud. When the probe intensity I_0 is much smaller than the saturation intensity, the second term in Eq. 3.4 becomes negligible. Assuming further that the probe light is on resonance, $\delta = 0$, the atomic column density becomes simply $\sigma_0 n = OD$. Figure 1b shows a Gaussian atomic density distribution (top) and the resulting probe intensity as a function of position in the cloud (bottom). The intensity drops from its initial to final value gradually as it traverses the cloud.

However, there is an important effect that the above equations do not account for. Namely, as the atoms absorb light from the probe beam, they also get a momentum kick equal to the momentum of a photon during each collision $\hbar k_r = h/\lambda_L$ in the direction of propagation. It is true that the absorbed photon will then be re-emitted by the atom, inducing a loss of momentum, but since this happens through the process of spontaneous emission into a random vacuum mode, the average momentum kick acquired this way over many re-emissions will average to zero. On average, each photon absorbed will induce a change in velocity of the atom of $v_r = \hbar k_r/m$,

where m is the atomic mass, as depicted in Fig. 1c. As the velocity of the atom changes, due to the Doppler effect, the apparent laser frequency will change as well. Therefore, even if the laser light is exactly on-resonant for a stationary atom, it will become off-resonant for longer imaging times, and Eq. 3.3 will acquire a time dependence. For most experiments, this effect is small and can be neglected. However, if the imaging time becomes of order a recoil time t_r, a time after which the recoil-induced detuning δ becomes of order Γ, this effect becomes significant. We explore this effect in Chapter 4.

3.2.1 Time-of-flight and in situ imaing

There are two commonly used protocols for measuring cold atomic clouds, in situ and time of flight measurements. Generally, the atomic cloud is trapped (in our case by an optical dipole trap) during the experiment. In situ is Latin for in its original place. As suggested by the name, in situ measurements are taken while the cloud is still in its original trap, or immediatly after the trap is turned off before any dynamics have had time to occur. These measurments measure the real spatial distribution of the atoms at the end of the given experiment. There is a difficulty asscoiated with making in situ measurments of BECs, however. Namely, BECs in their original trap tend to be relatively dense, with optical depths often in excess of $OD \approx 20$, requiring unrealistic probe light intensities to resolve. One way to bypass this difficulty is to selectively image only a small fraction of the condensed atoms, as was done with microwave imaging for our magnetic field stabilization feedforward protocol [INSERT SECTION REFERENCE HERE ONCE ITS WRITTEN]. Another option is to instead perform a time-of-flight measurement.

In time-of-flight measurements, the trapping potential is abruptly snapped off after the experiment, and the atoms are allowed to free fall and expand for some time t. For our experiments, t was on the order of tens of miliseconds. In the

regime where time t is long enough that the atoms travel much further than the initial extent of the cloud in the directions transverse to the imaging axis, the final position of the atoms is determined almost exclusively by their in situ momentum, not their in situ position. Therefore, time-of-flight imaging in this regime measures the atomic distribution as a function of momentum, not position.

3.3 One dimensional optical lattices

3.3.1 Far off-resonant atom-light interaction

As described in section 3.1, on timescales where spontaneous emission can be neglected, two-level atoms exposed to laser radiation undergo coherent Rabi oscillations between the two levels. Starting with c_g and c_e as the time-dependent coefficients multiplying the eigenstate wavefuntions of the ground and excited state respectively, and assuming the atom starts in the ground state $c_g(t = 0) = 1$, we make the traditional transformation to the rotating frame:

$$c'_g(t) = c_g(t) \tag{3.5}$$

$$c'_e(t) = c_e(t)e^{-i\delta t}, \tag{3.6}$$

where δ is the detuning of laser light from resonance. In this frame, we can write the atom-light Hamiltonian in the $\begin{pmatrix} c'_g \\ c'_e \end{pmatrix}$ basis as:

$$H = \hbar \begin{pmatrix} -\delta/2 & \Omega/2 \\ \Omega/2 & \delta/2 \end{pmatrix}, \tag{3.7}$$

where Ω is the coupling strength, also known as the Rabi frequency. In the limit of no coupling, $\Omega = 0$, in the rotating frame the eigenenegies are $E_\pm = \pm\hbar\delta/2$.

For non-zero coupling, finding the eigenvalues of H gives $E_\pm = \pm\hbar\sqrt{\delta^2 + \Omega^2}/2$. Therefore, the bare (without light) eigenenrgies are shifted in the presence of the light.

For a far detuned laser beam, one expects that no absorption of the light will actually take place, and the atom will remain entirely in the ground state. Indeed, solving the Shroedinger equation with the above Hamiltonian

$$i\hbar\frac{d}{dt}\begin{pmatrix} c_g' \\ c_e' \end{pmatrix} = H \begin{pmatrix} c_g' \\ c_e' \end{pmatrix} \tag{3.8}$$

we obtain the oscillating excited state population

$$c_e'(t) = -i\frac{\Omega}{\sqrt{\Omega^2 + \delta^2}}\sin\left(\frac{\sqrt{\Omega^2 + \delta^2}t}{2}\right), \tag{3.9}$$

where the amplitude of the oscillation approches zero in the limit $\Omega \ll \delta$. Thus, the only effect of the light in this regime is to shift the eigenenergies of the ground and excited states. Expanding the energies in the small parameter Ω/δ, we obtain the shifted energies $E_\pm = \pm\hbar\sqrt{\delta^2 + \Omega^2}/2 \approx \pm(\delta/2 + \Omega^2/4\delta)$. The shift from bare energy levels is thus

$$\Delta E_\pm = \pm\Omega^2/4\delta. \tag{3.10}$$

This laser intensity dependent energy shift is called the AC Stark shift, and is the basis of most laser created potentials for cold atoms.

For the ground state, and a red detuned laser beam (where the laser frequency is lower than the resonant frequency), this creates energy minima in locations of maximal laser intensity. For the lattice described in this chapter, as well as for the trapping of our atoms in the final stages of cooling, we use high power (up to 10 W) lasers with wavelength $\lambda_L = 1064$ nm.

3.3.2 Lattice Hamiltonian

Our 1-D optical lattice is created by retro-reflecting the $\lambda_L = 1064$ nm laser, creating a standing wave of light. Via the AC Stark shift, this creates a periodic potential for the atoms of the form

$$V = V_0 \sin^2(k_L x), \tag{3.11}$$

where $k_L = 2\pi/\lambda_L$ is the wavenumber associated with the lattice recoil momentum. The time-independent Hamiltonian, for some eigenenergy E_n, will be given by

$$-\frac{\hbar^2}{2m}\frac{d^2}{dx^2}\Psi_n(x) + V_0\sin^2(k_L x)\Psi_n(x) = E_n\Psi_n(x). \tag{3.12}$$

Since the potential is spatially periodic, we can invoke Bloch's theorem [5]:

$$\Psi_{n,q} = e^{iqx}u_{n,q}(x), \tag{3.13}$$

where q is the crystal momentum restricted to $\pm\hbar k_L$, and $u_{n,q}(x)$ is the spatially varying part of the wavefunction. Plugging this in to the Hamiltonian, we obtain

$$-\frac{\hbar^2}{2m}\left(-q^2 + 2iq\frac{d}{dx} + \frac{d^2}{dx^2}\right)u_{n,q}(x) + V_0\sin^2(k_L x)u_{n,q}(x) = E_n u_{n,q}(x). \tag{3.14}$$

Expanding $u_{n,q}(x)$ in Fourier components commensurate with the lattice period of $2k_L$ as $u_{n,q}(x) = \sum_{j=-\inf}^{\inf} a_j e^{i2k_L jx}$, we obtain

$$\sum_j \left(\frac{\hbar^2}{2m}(q+2k_L)^2 a_j + V_0\sin^2(k_L x)a_j\right)e^{i2k_L jx} = E_n\sum_j a_j e^{i2k_L jx}. \tag{3.15}$$

Re-writing $\sin^2(k_L x) = (e^{-2ik_L x} + e^{2ik_L x} - 2)/4$, multiplying both sides by $e^{i2k_L j'x}$ and invoking $\sum c_j e^{ik(j-j')} = \delta_{jj'}$, where $\delta_{jj'}$ is the Kroniker delta and c_j are appropriately

normalized coefficients, we get for any value of the index j

$$\frac{\hbar^2}{2m}(q + 2k_L j)^2 a_j - \frac{V_0}{4}(a_{j+1} + a_{j-1}) = E_n a_j. \tag{3.16}$$

This can be expressed in matrix form

$$H_L = \begin{pmatrix} \ddots & & & & & \\ & \frac{\hbar^2}{2m}(q + 4k_L)^2 & \frac{V_0}{4} & 0 & 0 & 0 \\ & \frac{V_0}{4} & \frac{\hbar^2}{2m}(q + 2k_L)^2 & \frac{V_0}{4} & 0 & 0 \\ & 0 & \frac{V_0}{4} & \frac{\hbar^2}{2m}q^2 & \frac{V_0}{4} & 0 \\ & 0 & 0 & \frac{V_0}{4} & \frac{\hbar^2}{2m}(q - 2k_L)^2 & \frac{V_0}{4} \\ & 0 & 0 & 0 & \frac{V_0}{4} & \frac{\hbar^2}{2m}(q - 4k_L)^2 \\ & & & & & & \ddots \end{pmatrix}, \tag{3.17}$$

in the basis of momentum orders $|k\rangle = e^{ikx}$ given by:

$$\begin{pmatrix} \vdots \\ |q + 4k_L\rangle \\ |q + 2k_L\rangle \\ |q\rangle \\ |q - 2k_L\rangle \\ |q - 4k_L\rangle \\ \vdots \end{pmatrix}. \tag{3.18}$$

This matrix can be diagonalized for every value of the crystal momentum q, with the resulting band structure shown in Figure 2. It is convenient to define the lattice recoil energy $E_L = \hbar^2 k_L^2 / 2m$. Then, we can re-write the Hamiltonian with
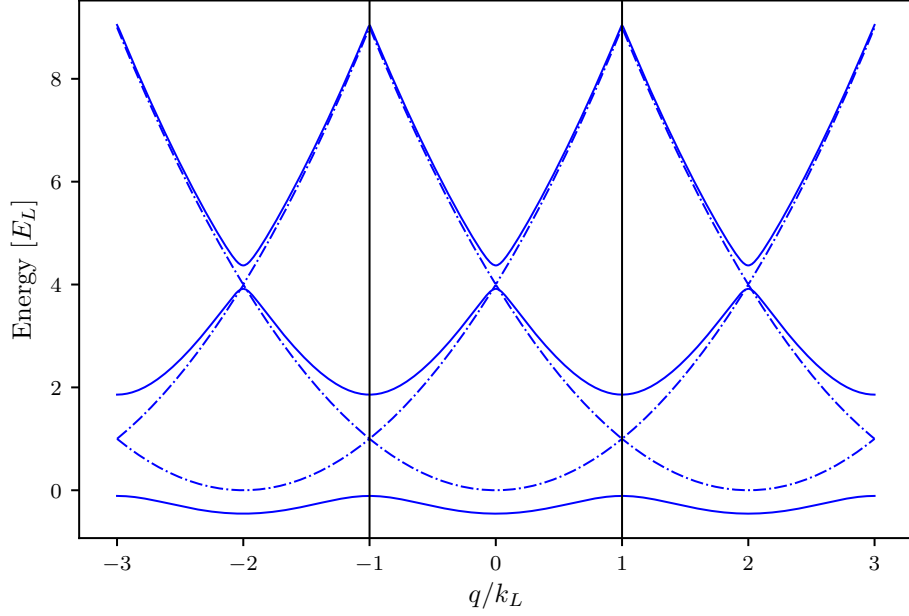
Figure 2: Lattice band structure in the extended zone scheme. The dashed lines represent the limit of zero lattice depth, with the regular parabolic dispersion relation of a free particle repating with reciprocal lattice period. The solid lines are the dispersion relation at $V_0 = 4.0E_L$, showing the opening of gaps at crossings of the zero lattice depth bands. The black lines demarcate the first Brillouin zone.

V_0 in units of E_L and momenta q in units of k_L as

$$H_L/E_L = \begin{pmatrix} \ddots & & & & & \\ & (q+4)^2 & \frac{V_0}{4} & 0 & 0 & 0 \\ & \frac{V_0}{4} & (q+2)^2 & \frac{V_0}{4} & 0 & 0 \\ & 0 & \frac{V_0}{4} & q^2 & \frac{V_0}{4} & 0 \\ & 0 & 0 & \frac{V_0}{4} & (q-2)^2 & \frac{V_0}{4} \\ & 0 & 0 & 0 & \frac{V_0}{4} & (q-4)^2 \\ & & & & & & \ddots \end{pmatrix}. \qquad (3.19)$$

In any numerical simulation, the number of momentum orders that can be included is finite. We determine the value of the parameter $n = \max(|j|)$ as the

lowest n at which the eigenvalues stop changing to machine precision from $n - 1$. The code for finding and plotting the eigenvalues and eigenvectors of the lattice hamiltonian is included in Appendix [MAKE APPENDIX WITH CODE?].

3.3.3 Tight binding approximation

In the limit of large lattice depths, $V_0 >\approx 5E_L$, the lattice Hamiltonian is well approximated by the tight-binding model. In the tight binding model, the basis is assumed to be a set of orthogonal functions, called Wannier functions, localized to each lattice site $|j\rangle$. The approximation lies in assuming only nearest neighbor tunnelings between the sites, forming the tight-binding Hamiltonian

$$H_{\text{tb}} = -t \, |j\rangle \, \langle j + 1| + \text{H.c.}, \tag{3.20}$$

where t is the tunneling amplitude between nearest neighbor sites and H.c. stands for Hermitian conjugate. We have neglected the diagonal kinetic energy term, as it will be equal for every Wannier function $|j\rangle$ and thus represents a constant energy offset. All the information about the lattice depth is therefore reflected in the tunneling amplitude t.

The tight binding Hamiltonian can also be expressed in the momentum basis by Fourier transforming the basis functions:

$$|j\rangle = \frac{1}{\sqrt{N}} \sum_{k_j} e^{-ik_j j} \, |k_j\rangle \,, \tag{3.21}$$

giving the Hamiltonian

$$H_{\text{tb}} = -\frac{1}{N} \sum_{k_1} \sum k_2 t e^{-ijk_1} e^{ik_2(j+1)} \, |k_1\rangle \, \langle k_2| + \text{H.c} = 2t\cos(k) \, |k\rangle \, \langle k| \,. \tag{3.22}$$

From this we can directly read off the band structure of the tight binding Hamilto-

nian. First, we notice that we only obtain one band - to approximate higher bands with the tight binding approximation we would need to construct a different set of Wannier functions and a different tunneling strength. Second, we see that the lowest band is simply a cosine - therefore we have solved for the band structure without even defining what the basis Wannier functions are! Third, the amplitude of the cosine function is given by the tunneling strength t. This gives us a good clue as to how to determine the appropriate tunneling given a lattice depth V_0 - simply find a t that matches the amplitude of the lowest band, which becomes cosinusoidal in the deep lattice limit.

The precise form of the Wannier functions depends on both the depth of the lattice and the band being reproduced. It is not necessary for us to find their full expression, as the band structure can be calculated without them. The definition, however, is

$$|j\rangle = \int_{\mathrm{BZ}} e^{i\phi(q)-iqja} \Psi_q(x)\mathrm{d}q, \tag{3.23}$$

where the integral is over the Brillouin zone, from $-k_L$ to k_L, a is the lattice spacing $\lambda_L/2$, and Ψ_q is the Bloch wavefunction at crystal momentum q, and $\phi(q)$ is the phase associated with each Bloch wavefuntion. The Bloch wavefunctions individually have arbitrary phase. The phase plays an important role in combining the Bloch wavefunctions into a Wannier function, finding the proper phase relationship to make the wavefunction maximally localized at each site [6].

3.3.4   Pulsing vs adiabatic loading of the lattice

The lattice depth parameter $V_0/4$, for a range of values, can be well calibrated experimentally by pulsing on the lattice. Here, the word pulsing indicates that the lattice is turned on fully non-adiabatically, if not instantaneously, such that the original bare momentum state is projected onto the lattice eigenbasis, as shown

in Figure 5a. If the atoms start out stationary in the trap, the bare state in the momentum basis is simply

$$|\Psi_0\rangle = \begin{pmatrix} \vdots \\ 0 \\ 0 \\ 1 \\ 0 \\ 0 \\ \vdots \end{pmatrix}, \tag{3.24}$$

as depicted in Figure 5b.

Since the lattice eigenbasis is distinct from the bare one, instiantaneously turning on the lattice will necessarily excite the atoms into a superposition of lattice eigenstates, each evolving with a different phase according to the eigenenergy while the lattice is on, as shown in Figure 5c. Then, when the lattice is snapped back off, the wavefunction is projected back into the bare basis, and the varying phase accumulation results in a beating of the different momentum orders, see Figure 5d. This can be calculated simply by using the time evolution operator

$$|\Psi(t)\rangle = e^{-iH_L t/\hbar} |\Psi_0\rangle. \tag{3.25}$$

By pulsing on the lattice for variable amounts of time t, we can obtain fractional populations in the different momentum states. Time-of-flight imaging captures the momentum distribution of the cloud, and the different entries of $\Psi(t)$ in the momentum basis will thus appear as different clouds on the absorption image, as shown in Figure 4a. The fractional population in these clouds corresponds to a measurement of $|a_j|^2$. Typically for our values of the lattice depth $V_0 < 10E_L$, it is sufficient to simply count three central momentum orders, $k = q, q \pm 2k_L$. Then, we can fit Eq.
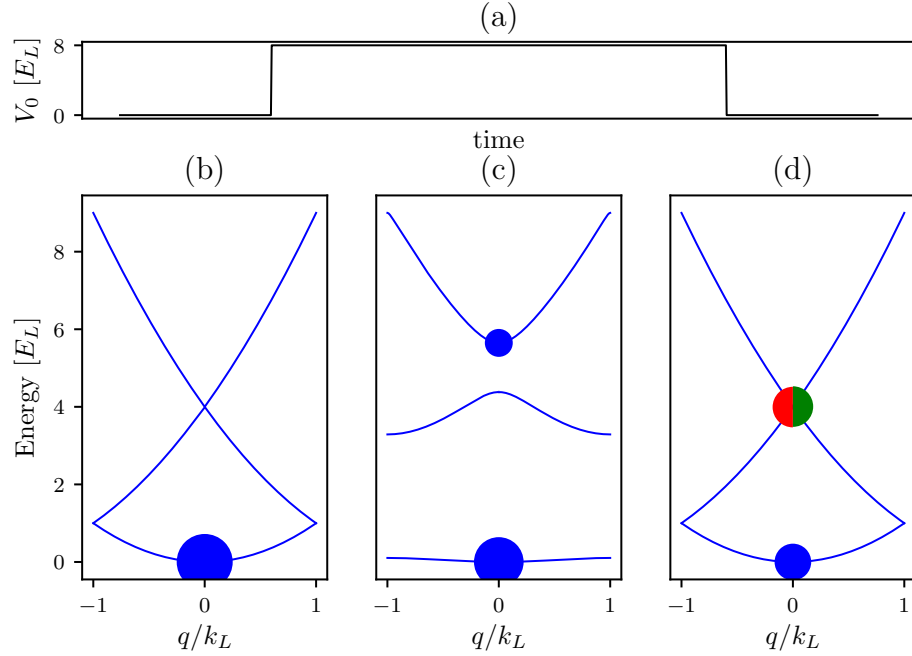
Figure 3: Lattice pulsing. (a) Lattice depth as a function of time during a pulsing experiment. The lattice is turned on instantaneously at $t = 0$ and held on for a variable amount of time until being turned off instantaneously at a final time $t = t_f$. (b) Atomic population before $t = 0$. The dispersion relation is that of a free particle, and all of the atoms start out at $q = 0$ in the lowest energy level. Here, the area of the dots is proportional to the fractional population in the energy state. (c) Atomic population after the lattice is turned on for a lattice depth of $V_0 = 8.0E_L$. The energy spectrum now shows the lattice band structure, and some atomic population is projected onto the excited bands. (d) Atomic population after the lattice is snapped off at $t_f = 150$ μs. The wavefunction is projected back onto the bare states, with some fraction (blue circle) in the lowest band at $k = 0$ and some fraction in the excited band, with equal population being projected onto the $k = 2k_L$ (green) and $k = -2k_L$ (red).
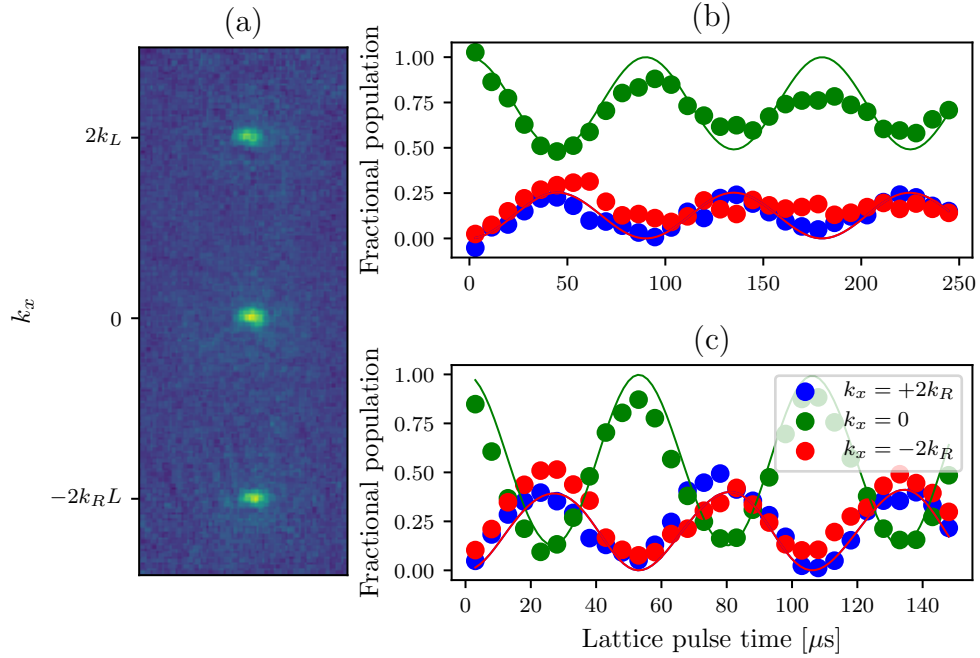
Figure 4: Lattice pulsing for calibration. (a) An example time-of-flight image from a pulsing experiment. The three different clouds are different momentum orders. (b) Fractional populations in the different momentum orders as a function of pulsing time at a low lattice power. Data is indicated by dots and best fit theory is represented by lines. The lattice depth from fit is $V_0 = 5.57 \pm 0.07 E_L$. (c)Fractional populations in the different momentum orders as a function of pulsing time at a higher lattice power. Data is indicated by dots and best fit theory is represented by lines. The lattice depth from fit is $V_0 = 12.69 \pm 0.07 E_L$.

3.25 to the data with fitting parameter V_0, thus deducing the lattuce depth. Some examples of these pulsing experiments are presented in figure 4b,c.

In contrast to pulsing, adiabatic loading turns the lattice on slowly, such that the atomic wavefunction starting in the bare ground state can continuously adjust to remain in the ground state of the current Hamiltonian, without projecting onto any of the higher bands. This process is illustrated in Figure 5. The adiabatic timescale depends on the spacing between the ground and next excited band (or if starting in a different eigenstate, the nearest eigenstate). If the energy difference between the ground and first excited state is ΔE, the timescale on which the lattice

is turned on must fullfill $t \gg h/\Delta E$.

3.4   Raman and rf coupling

3.4.1   Hyperfine structure

Alkali atoms' energy levels can be understood as primarily the energy state of the single electron in the outer shell. Fine structure arises from different combinations of angular momenta, including orbital angular momentum of the outermost electron with respect to the nucleus $\mathbf{L}$, the electron spin $\mathbf{S}$ and the nuclear spin $\mathbf{I}$. The total electron angular momentum is the combination of orbital and the spin angular momenta $\mathbf{J} = \mathbf{L} + \mathbf{S}$, and the quantum number can be any integer $|L - S| \leq J \leq |L + S|$. The ground state of ^{87}Rb, in term notation $^{2S+1}L_J$ is $^2S_{1/2}$, where S is orbital notation indicating $L = 0$. Since the total spin quantum number $J = 1/2$, this produces two possible spin projection quantum numbers, $m_J = \pm 1/2$.

There is also a contribution from the nuclear spin $\mathbf{I}$, resolvable at low magnetic fields, which gives rise to hyperfine structure of the states. For ^{87}Rb, $I = 3/2$. The total spin, including nuclear spin, is indicated by the quantum number F, and $|J - I| \leq F \leq |J + I|$. The interaction with the nuclear spin splits the ground state of ^{87}Rb into two manifolds, $F = 1$ and $F = 2$, with three hyperfine states in the $F = 1$ manifold ($m_F = 0, \pm 1$) and five hyperfine states in the $F = 2$ manifold ($m_F = 0, \pm 1, \pm 2$). These states couple to an external magnetic field B_z along some direction $\mathbf{e}_z$ via the Hamiltonian $H_B = \mu_B(g_J J_z + g_I I_z)B_z/\hbar$. Here μ_B is the Bohr magneton, and g_J and g_I are Lande g-factors. Since $g_J \gg g_I$, at high fields the nuclear spin interaction becomes small compared to the total energy shift, and the levels are grouped according to their m_J quantum number, as seen in Figure 6.

At low fields, however, the states are approximately linearly dependent on the m_F quantum number. The linear shift from the $B = 0$ states is known as the linear
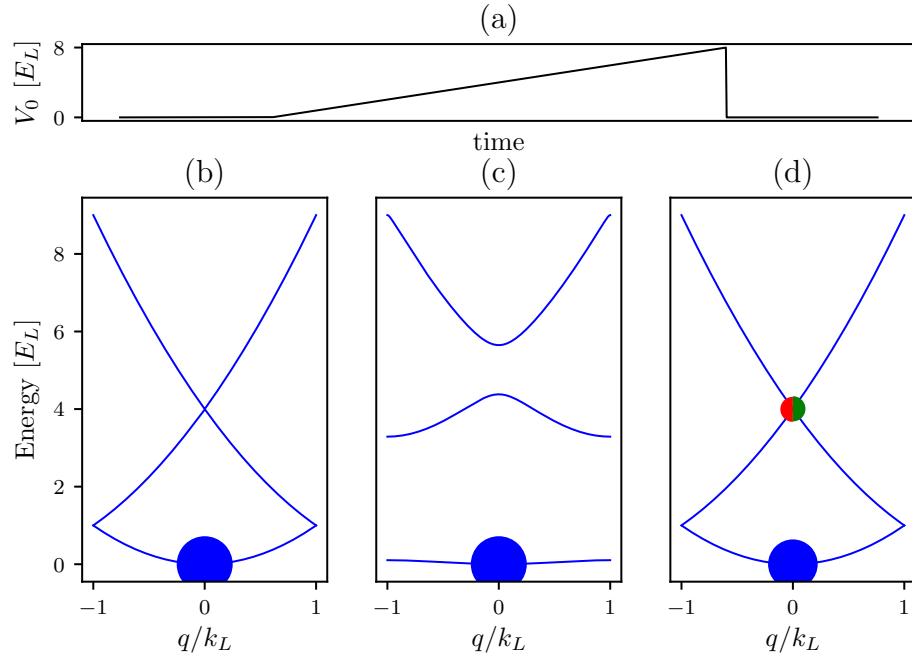
Figure 5: Adiabatic lattice loading. (a) Lattice depth as a function of time during adiabatic turn-on. The lattice is ramped on starting at $t = 0$, slowly increasng to a final lattice depth and turned off instantaneously at a final time $t = t_f$. (b) Atomic population before $t = 0$. All atoms are at $k = 0$ in the lowest bare band. (c) Atomic population after the lattice is turned on adiabatically to a lattice depth of $V_0 = 8.0E_L$. All atoms remain in the lowest band, but the band is no longer bare. (d) Atomic population after the lattice is snapped off. The wavefunction is projected back onto the bare states, with some fraction (blue circle) in the lowest band at $k = 0$ and some fraction in the excited band, with equal population being projected onto the $k = 2k_L$ (green) and $k = -2k_L$ (red). Since the lowest lattice band is a superposition of bare bands, some atoms are excited to the higher bare bands.
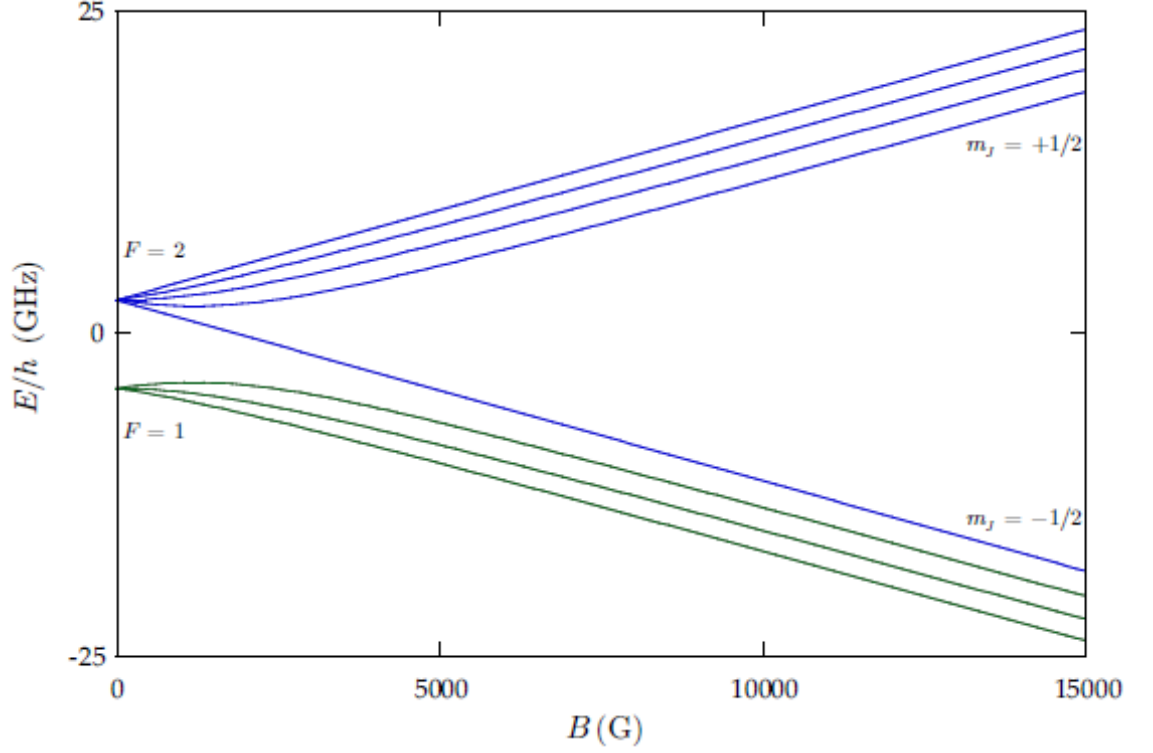
Figure 6: Energy structure of hyperfine states of the ground state of ^{87}Rb as a function of external magnetic field strength in Gauss. Figure from ref. [2]

Zeeman shift. In the intermediate regime, the correction to the linear shift can be expressed in terms of and energy correction to each hyperfine state $\epsilon(B)|m_F|^2$, known as the quadratic Zeeman shift. For the magnetic fields used in experiments described in this thesis, this correction is sufficient for describing the energy levels.

The form of the Hamiltonian in this regime for any value of F is given by

$$H_0 = H_{\mathrm{KE}} + \hbar\omega_z \mathbf{F_z} + \hbar\epsilon \mathbf{F_z}^2, \tag{3.26}$$

where $\hbar\omega_z = \mu_B g_F B_z/\hbar$, and the kinetic energy Hamiltonian $H_{\mathrm{KE}} = \hbar^2\vec{k}^2/2m\mathcal{I}$, and $\mathcal{I}$ is the identity matrix.

3.4.2 Rf coupling Hamiltonian

For the $F = 1$ manifold, there are three available spin states $m_F = 0, \pm 1$. There are many ways of introducing coupling terms between the different hyperfine states. Here, we will explain two methods: rf coupling and Raman coupling. Rf coupling is a radio-frequency oscillating magnetic field, in our case produced by a pair of circular coils in series side by side above the atoms (see [7]). Assuming the rf oscillating field is polarized along the $\mathbf{e}_x$, with the bias field along $\mathbf{e}_z$, the coupling Hamiltonian is given by $H_{rf} = \mu_B g_F \vec{\mathbf{F}} \cdot \vec{B} = \mu_B g_F \mathbf{F}_x B_x \cos(\omega t)$, where $2\pi\omega$ is the rf frequency. The schematic of this setup is shown in Figure 7. The eignestates of the bare Hamiltonian H_0 are the constituent m_F states. The eigenstates of the coupled Hamiltonian $H_0 + H_{rf}(t)$ can be expressed as a linear superposition of the bare eignestates $\Psi(\vec{x}, t) = \sum_{m_F} c_{m_F}(t) \phi_{m_F}(\vec{x}) e^{-i\omega_{m_F} t}$. The Hamiltonian in this basis can then be written as [4]

$$
H_{\text{rf}} = H_{\text{KE}} + \hbar \begin{pmatrix} 0 & \Omega\cos(\omega t)e^{i\omega_z t} & 0 \\ \Omega\cos(\omega t)e^{-i\omega_z t} & 0 & \Omega\cos(\omega t)e^{i\omega_z t} \\ 0 & \Omega\cos(\omega t)e^{-i\omega_z t} & 0 \end{pmatrix}, \qquad (3.27)
$$

where Ω is the Rabi frequency, proportional to B_x. We can then transfer into the rotating frame $c'_{m_F} = e^{-im_F \delta t} c_{m_F}$, where $\delta = \omega_z - \omega$. Then we apply the rotating wave approximation, that the fast oscillating terms average to zero over time scales of interest $e^{2i\omega t} \approx 0$, and obtain

$$
H_{\text{rf}} = H_{\text{KE}} + \hbar \begin{pmatrix} \delta & \Omega/2 & 0 \\ \Omega/2 & -\epsilon & \Omega/2 \\ 0 & \Omega/2 & -\delta \end{pmatrix}, \qquad (3.28)
$$
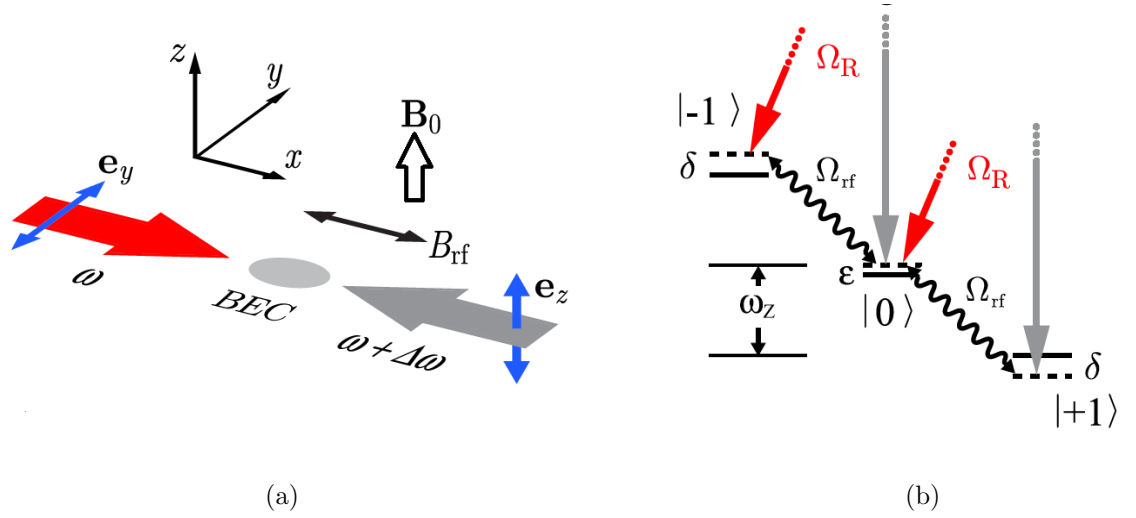
Figure 7: Raman and rf coupling schematic. (a) Beam geometry of the Raman beams and rf relative to the external field. The Raman beams have a frequency difference $\Delta\omega$, and are linearly polarized in perpendicular directions. (b) Level structure of both Raman and Rf coupling for hyperfine states of the $F = 1$ manifold. The hyperfine splitting sparates the levels by an energy $\hbar\omega_z$. The quadratic Zeeman shift ϵ lowers the energy of the $m_F = 0$ state, and the detuning δ of either the Raman or the rf fields shifts the energies of the $m_F = \pm 1$ states. Raman transitions are two-photon, exciting up to a virtual state and coming back down to an adjacent hyperfine state, with an accompanying momentum transfer. Rf couples adjacent hyperfine states directly. Figure taken from ref. [3]

or for any value of F

$$H_{\text{rf}} = H_{\text{KE}} + \hbar\delta F_z + \hbar\epsilon F_z^2 + \Omega F_x/2. \tag{3.29}$$

The band structure of this Hamiltonian can be seen in Figure 8, where we have diaganolized Eq. 3.28 for a range of momenta k_x (we have islolated k_x for comparison with Raman coupling, as will be seen in the next section). The parabolas are simply the free particle dispersion relations along one dimension, with three bands arising from the three available spin states. It is convenient to define the magnetization of an eigenstate $m = \sum_{m_F} m_F * p_{m_F}$, where p_{m_F} is the fractional population in the m_F state. We have indicated the magnetization of the eigentate by coloring the

eigenenrgies, with $m = -1$ in red, $m = 0$ in green, and $m = +1$ in blue. In Figure 8a, both the detuning and the coupling strength are zero. Therefore, there are simply three free particle dispersions, each exactly correlated with a particular spin state, the $m_F = \pm 1$ are degenerate and the $m_F = 0$ state is slightly offset by the quadratic shift $\hbar \epsilon$. In Figure 8c, the coupling strength is again zero, but the detuning has been turned on, lifting the degeneracy between the $m_F = \pm 1$ states. Figure 8b,d shows the same conditions as a,c, respectively, but with the coupling strength turned on. In Figure 8b, where the detuning is zero and the quadratic shift is negligible compared to the coupling strength, all states average to a magnetization of zero–the $m_F = \pm 1$ states are symmetrically populated. In Figure 8d, this symmetry is broken by the presence of a detuning.

3.4.3 Raman coupling Hamiltonian

The counter-propagating Raman beams, as seen in Figure 7, couple the same states as the rf. The do so via the vector light shift created by the pair of beams. The electric field due to the right going beam (red in Figure 7a) is $\mathbf{E} = E_0 \exp(ik_R x - i\omega t)\mathbf{e}_y$, where E_0 is the amplitude of the electric field and $\hbar k_R = h/\lambda_R = \hbar\omega/c$. The electric field from the left going beam (gray in Figure 7b) is $\mathbf{E} = E_0 \exp(-ik_R x - i(\omega + \Delta\omega)t)\mathbf{e}_z$. This combines to give an effective field from the vector light shift [8] $B_{\text{eff}} \propto \mathbf{E} \times \mathbf{E}^* \propto -E_0^2 \cos(2k_R x + \Delta\omega t)\mathbf{e}_x$. Going through the same procedure as for the rf coupling case, including the transfer into the rotating frame and the rotating wave approximation, we obtain the same Hamiltonian in the basis of bare spin states $|-1\rangle, |0\rangle, |1\rangle$ but with an extra phase factor:

$$
H_{\text{Raman}} = H_{\text{KE}} + \hbar \begin{pmatrix} \delta & \Omega/2 e^{-i2k_R x} & 0 \\ \Omega/2 e^{i2k_R x} & -\epsilon & \Omega/2 e^{-i2k_R x} \\ 0 & \Omega/2 e^{i2k_R x} & -\delta \end{pmatrix}, \qquad (3.30)
$$
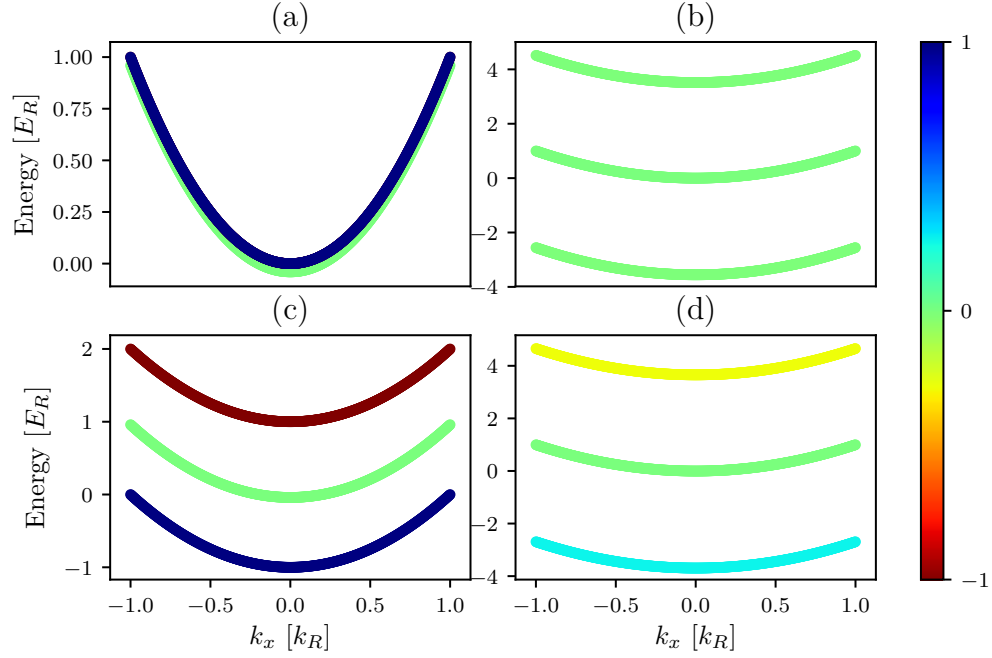
Figure 8: Band structure of the rf Hamiltonian, Eq. 3.28, in momentum space. For all plots, the quadratic Zeeman shift $\hbar\epsilon = 0.04E_R$, and the color represents magnetization, labeled by the colorbar. (a) $\hbar\Omega = 0$, $\hbar\delta = 0$. No coupling or detuning is present, so the only separation between the bands is due to the quadratic shift $\hbar\epsilon$. (b) $\hbar\Omega = 5.0E_R$, $\hbar\delta = 0$. (c) $\hbar\Omega = 0$, $\hbar\delta = 1.0E_R$. Even though the coupling strength is zero, the bands are separated by the detuning. (d) $\hbar\Omega = 5.0E_R$, $\hbar\delta = 1.0E_R$.

where $\delta = \omega_z - \Delta\omega$.

This phase difference between the rf and Raman Hamiltonian has an intuitive physical explanation. In order to undergo a Raman transition, an atom first absorbs a photon from one beam, getting a momentum kick equal to the recoil momentum $\hbar k_R$. Then, to decay back down to an adjacent spin state, the undergoes stimulated emission into the field of the other (counter-propagating) beam, acquiring another recoil momentum kick in the same direction for a total of $2\hbar k_R \mathbf{e}_x$. Therefore, the Raman coupling Hamiltonian for $F = 1$, after transforming into the rotating frame and performing the rotating wave approximation, can be written in the same way as the rf Hamiltonian in Eq. 3.28 with the addition of a momentum kick—in real space, an aquired phase—of $e^{i2k_R x}$.

We can again make a basis transformation to get rid of this phase. Let us define $|-1\rangle' = \exp(-2ik_R x)|-1\rangle = |k_x - 2k_R, -1\rangle$, $|0\rangle' = |0\rangle = |k_x, 0\rangle$, $|1\rangle' = \exp(2ik_R x)|1\rangle = |k_x + 2k_R, 1\rangle$, where for third definition we went into the momentum basis and labelled the states by a combination of their momentum and spin state. Then, including the kinetic energy term along $\mathbf{e}_x$ explicitly, we obtain the Hamiltonian in the new basis as:

$$H_{\text{Raman}} = H_{\text{KE}}^{(y,z)} + \begin{pmatrix} \frac{\hbar^2(k_x - 2k_R)^2}{2m} + \hbar\delta & \hbar\Omega/2 & 0 \\ \hbar\Omega/2 & \frac{\hbar^2 k_x^2}{2m} - \hbar\epsilon & \hbar\Omega/2 \\ 0 & \hbar\Omega/2 & \frac{\hbar^2(k_x + 2k_R)^2}{2m} - \hbar\delta \end{pmatrix}. \quad (3.31)$$

It is convenient to define the Raman recoil energy as $E_R = \frac{\hbar^2 k_R^2}{2m}$. The band structure of this Hamiltonian is shown in Figure 9, for several representative parameter values, with the magnetization labelled by the color. Figure 9a shows the band structure in the limit of zero coupling and zero detuning, but where we have already gone into the basis $|k_x - 2k_R, -1\rangle$, $|k_x, 0\rangle$, $|k_x + 2k_R, 1\rangle$; therefore, the free particle parabola corresponding to the $m_F = 1$ spin states is shifted to center on

$k_x = -2k_R$ and the $m_F = -1$ parabola is shifted to center on $k_x = 2k_R$. As the coupling is turned on to $\hbar\Omega = 1E_R$ in Figure 9b, the points where the parabolas cross become 'avoided crossings', separating into three bands where magnetization (and the underlying spin distribution) depends on the momentum k_x. As the coupling strength is turned up even further to $\hbar\Omega = 5E_R$ in Figure 9c, the lowest band goes from having three minima, one corresponding to each original spin state, to only one minimum. This transition happens at $\hbar\Omega = 4E_R$ [7]. In Figure 9d, we show the band structure again in the limit of zero coupling, but this time with a detuning of $\hbar\delta = 1.0E_R$. Note that the detuning tips the parabolas with respect to each other. Figure 9e shows the detuned system with coupling strenth turned up to $\hbar\Omega = 1E_R$, still in the three minima regime but with avoided crossings creating three momentum and spin coupled bands. In Figure 9f, the detuned system is turned up to a coupling strength of $\hbar\Omega = 5E_R$, creating a single minimum, this time offset from $k_x = 0$.

We can write the general F version of the Raman coupled Hamiltonian in the basis $|k_x + m_F * 2k_R, m_F\rangle$, where $-F \leq m_F \leq F$, as:

$$H_{\text{Raman}} = H_{\text{KE}}^{(y,z)} + \hbar^2(k_x\mathcal{I} + 2k_RF_z)^2/2m + \hbar\delta F_z + \hbar\epsilon F_z^2 + \Omega F_x/2. \qquad (3.32)$$

3.4.4 Calibration of Raman and Rf dressed states

To calibrate the rf and Raman coupling strengths, we take a similar approach to the 1-D lattice calibration: start in a pure spin state, for example $m_F = 0$, and turn the coupling on non-adiabatically to induce Rabi oscillations between the coupled states. Then, during time-of-flight, apply a Stern-Gerlach gradient pulse to separate the spin compoenets and observe the fractional populations in different spin states as a function of Rabi oscillation time.

Figure 10a,b shows example images obtained in time-of-flight when pulsing on
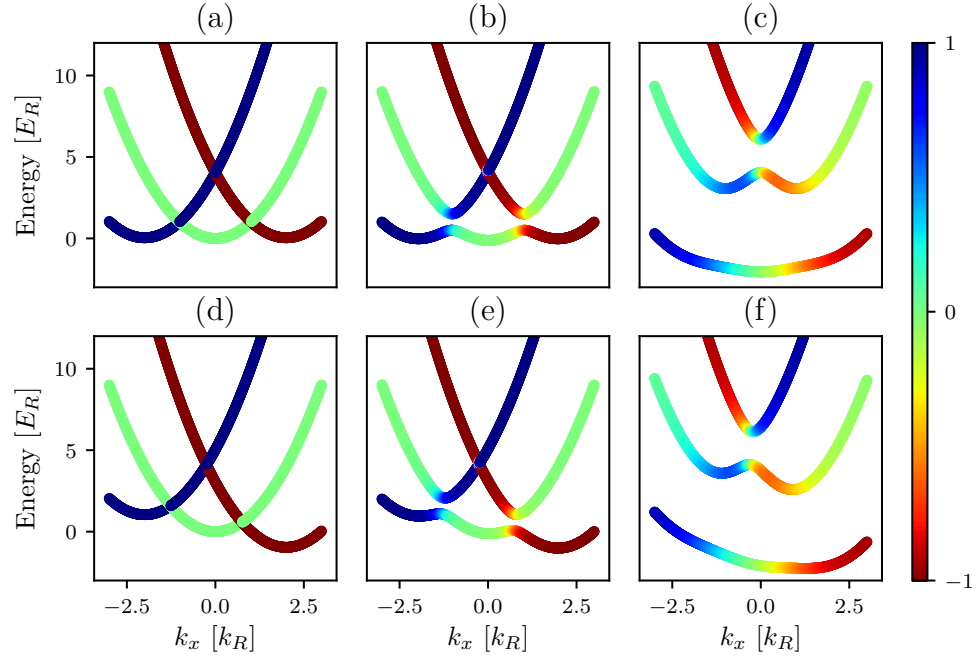
Figure 9: Band structure of the Raman Hamiltonian, Eq. 3.31, in momentum space. For all plots, the quadratic Zeeman shift $\hbar\epsilon = 0.04E_R$, and the color represents magnetization, labeled by the colorbar. (a) $\hbar\Omega = 0$, $\hbar\delta = 0$. (b) $\hbar\Omega = 1.0E_R$, $\hbar\delta = 0$. (c) $\hbar\Omega = 5.0E_R$, $\hbar\delta = 0.0$. (d) $\hbar\Omega = 0.0$, $\hbar\delta = 1.0E_R$. (e) $\hbar\Omega = 1.0E_R$, $\hbar\delta = 1.0E_R$. (f) $\hbar\Omega = 5.0E_R$, $\hbar\delta = 1.0E_R$

an rf coupling field for atoms in the $F = 1$ and $F = 2$ manifold, respectively. The Stern-Gerlach gradient pulse separates the spin components along the horizontal axis in the images. The fractional population in each state can then be obtained by summing up the optical depth in each cloud and dividing by the total optical depth. Similarly, Figure 11a shows an example time-of-flight image obtained when pulsing on a Raman coupling field on an $F = 1$ cloud initially in the $m_F = 0$ spin state. Here, the spin states are separated along the horizontal axis by the same Sternch-Gerlach pulse. In addition, the recoil momentum obtained when undergoing a Raman transition separates the different spin states along the vertical axis— parallel to the Raman beams along $\mathbf{e}_x$. The direction of the Stern-Gerlach gradient was chosen purposefully to be perpendicular to the Raman direction $\mathbf{e}_x$ for easy separation of the two effects.

These population oscillations can then be fit for coupling strength $\hbar\Omega$ and detuning $\hbar\delta$ Note that the quadratic Zeeman shift $\hbar\epsilon$ is set by the strength of the bias field B_0 and therefore often well known - we do not fit for this. The theoretic predictions are obtained by applying the time evolution operator $U = \exp(-iH_{\text{Raman/rf}}t/\hbar)$ to an initial state Ψ in the appropriate basis. Figure 10c shows an example time series of rf pulsing in the $F = 1$ maifold, starting in the $m_F = 0$ state. The lines of best fit are overlayed on experimental data, extracting fit parameters $\hbar\Omega = 0.863 \pm 0.004E_R$ and $\hbar\delta = -0.198 \pm 0.007E_R$. Figure 10d shows an example time series of rf pulsing in the $F = 2$ maifold, starting in the $m_F = -2$ state. Here, the extracted fit parameters were $\hbar\Omega = 1.000 \pm 0.002E_R$ and $\hbar\delta = -0.061 \pm 0.001E_R$.

Figure 11b shows an example time series of Raman pulsing in the $F = 1$ manifold, starting in the $m_F = 0$ state, with fitted parameters $\hbar\Omega = 1.47 \pm 0.01E_R$ and $\hbar\delta = 0.004 \pm 0.024E_R$. Note that although the coupling strength is almost double the rf coupling strenth in Figure 10c, the contrast (peak to peak oscillation
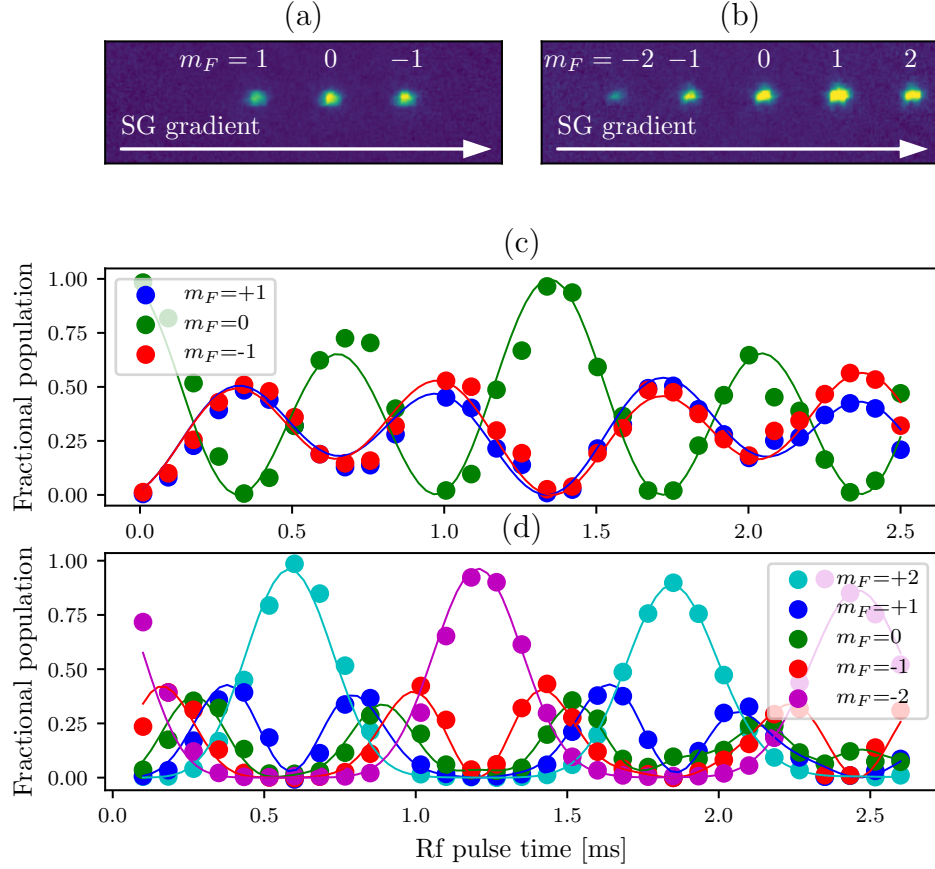
Figure 10: Pulsing on rf coupling. (a) Example time-of-flight image during an rf pusling experiment in the $F = 1$ manifold. Spin states are separated via a Stern-Gerlach pulse along the horizontal direction. (b) Example time-of-flight image during an rf pusling experiment in the $F = 2$ manifold. Here, 5 spin components are present. (c) Pulsing experiment in the $F = 1$ manifold. Dots represent fractional populations in different spin states measured from time-of-flight images, and lines repressent best fit theory curves. Fitted parameters are $\hbar\Omega = 0.863 \pm 0.004 E_R$, $\hbar\delta = -0.198 \pm 0.007 E_R$. (d)Pulsing experiment in the $F = 2$ manifold. Dots represent fractional populations in different spin states measured from time-of-flight images, and lines repressent best fit theory curves. Fitted parameters are $\hbar\Omega = 1.000 \pm 0.002 E_R$, $\hbar\delta = -0.061 \pm 0.001 E_R$. $\hbar\epsilon = 0.038 E_R$ for all panels.
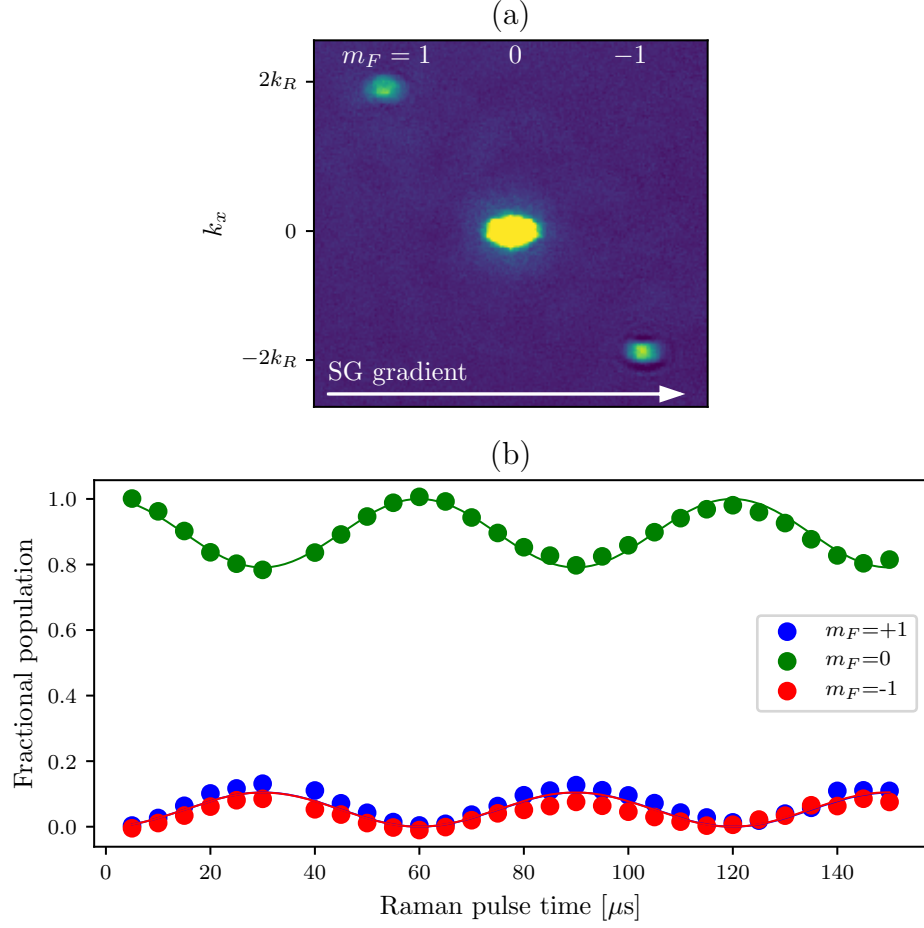
Figure 11: Pulsing on Raman coupling. (a) Example time-of-flight image during a Raman pulsing experiment in the $F = 1$ manifold. A Stern-Gerlach pulse during time-of-flight separates different spin components along the horizontal direction, and different momentum orders fly apart along the vertical direction. (b) Fractional population in different spin states during a Raman pulsing experiment as a function of time. Dots represent data and lines represent a best fit from theory. The fitted parameters are $\hbar\Omega = 1.47 \pm 0.01 E_R$, $\hbar\delta = 0.004 \pm 0.024 E_R$. The quadratic Zeeman shift was $\hbar\epsilon = 0.038 E_R$.

of the fractional population in, say, the $mF = 0$ state) is much lower in the Raman data than in the rf. This is a direct consequence of the recoil momentum transfer, and can be understood by looking at the band structure. For rf, the coupled bands at initial momentum $k_x = 0$ are separated by the coupling strength, see Figure ??b. For Raman, even at zero coupling strength, due to the shifting of the parabolas by $2k_R$, and $k_x = 0$ the higher bands are $\hbar^2(2k_R)^2/2m = 4E_R$ separated from the lower bands. Therefore, the energy difference is larger and the fraction in the excited band will be lower, leading to lower contrast.

Chapter 4: Absorption Imaging with Recoil Induced Detuning

In this Chapter, we describe the simulations we performed in order to interpret absorption images in a non-standard regime: at long imaging times, where the recoil induced detuning needed to be taken into account. This simulation was necessary to interpret data collected for our s-wave scattering experiment, described in Chapter 5. In this Chapter, we first describe the recoil-induced detuning effect and derive the equations to be solved. Then, we attempt to solve these equations perturbatively, and show that this treatment is insufficient in the regime of interest. We then perform two versions of the numberical simulations: one where the atoms are assumed to remain stationary relative to each other during imaging, and one where they are free to move. We show that although the atoms do move significantly during the imaging time, this does not have a strong effect on the final observed intensity. Finally, we use our simulated results to calibrate the saturation intensity in our camera units, and find the parameters for optimal signal-to-noise (SNR) ratio imaging. This work was previously reproted in [9].

4.1 Recoil-induced detuning

After absorbing a number of photons N, an atom will obtain a recoil velocity of $N v_{\mathrm{r}}$. Via the Doppler effect, this will result in a detuning $\delta = N k_{\mathrm{r}} v_{\mathrm{r}}$. This detuning will increase as more atoms are absorbed, and therefore depend on time, making the absorbed intensity also time dependent. We can generalize Eq. 3.3 to

include a time dependence on the detuning term and therefore also the intensity:

$$\frac{d}{dz}\frac{I(z,t)}{I_{\text{sat}}} = -\rho(z)\sigma_0\frac{I(z,t)/I_{\text{sat}}}{1 + 4\delta(z,t)^2/\Gamma^2 + I(z,t)/I_{\text{sat}}}. \tag{4.1}$$

The number of photons absorbed per atom will depend on the intensity lost, up until the current time, at that location. The detuning will therefore be proportional to the total number of photons lost up until time t at that location, proportional to the absorbed intensity divided by the single photon energy $\hbar\omega_L$, divided by the number of atoms that participated in the aborption $\rho(z)$ times the detuning $k_r v_r$:

$$\delta(t,z) = \frac{k_r v_r}{\hbar\omega_L\rho(z)}\int_0^t \frac{dI(z,\tau)}{dz}\mathrm{d}\tau. \tag{4.2}$$

These equations are interdependent, and cannot be in general solved analytically.

Figure 1a shows the velocity and detuning as a function of position in space for three different imaging times, calculated numberically. All calculations in this chapter were done for a cloud of ^{40}K atoms, as that is relevant to our experiment described in the next chapter. The resonant wavelength is $\lambda_L = 770.11$ nm, the natural linewidth of the transition is $\Gamma = 6.035$ MHz, the resulting saturation intensity and recoil velocity are $I_{\text{sat}} = 17.5$ W/m^2 and $v_r = 0.01297$ m/s.

4.2 Perturbative treatment

We can treat these equations perturbatively in time. To first order, we can set the detuning in Eq. 4.1 to $\delta = 0$, assume $I(z)$ is time independent, and plug that into Eq. 4.2 to obtain

$$\delta(t,z) = \frac{k_r v_r}{\hbar\omega_L\rho(z)}\int_0^t -\rho(z)\sigma_0\frac{I(z)}{1 + I(z)/I_{\text{sat}}}\mathrm{d}\tau \tag{4.3}$$

$$= \frac{k_r v_r \sigma_0}{\hbar\omega_L}\frac{I(z)}{1 + I/I_{\text{sat}}}t. \tag{4.4}$$

This can then be recursively plugged into Eq. 4.1 to obtain

$$\frac{d}{dz}\frac{I(z,t)}{I_{\text{sat}}} = -\rho(z)\sigma_0\frac{I(z,t)/I_{\text{sat}}}{1 + 4\left(\frac{k_r v_r \sigma_0}{\hbar\omega_L\Gamma}\frac{I(z)}{1+I/I_{\text{sat}}}\right)^2 t^2 + I(z,t)/I_{\text{sat}}}. \tag{4.5}$$

Integrating both sides of the above equation, we obtain a perturbative equation to second order in time [10]:

$$\sigma_0 n = ln(I_0/I_f) + \frac{I_0 - I_f}{I_{\text{sat}}} + \frac{(k_r v_r t)^2}{3}\left(\frac{I_{\text{sat}}}{I_f + I_{\text{sat}}} - \frac{I_{\text{sat}}}{I_0 + I_{\text{sat}}} + \ln\left(\frac{I_f + I_{\text{sat}}}{I_0 + I_{\text{sat}}}\right)\right). \tag{4.6}$$

In Fig. 1b, we examine for what imaging times the above perturbative equation, as well as the modelt that completely ignores recoil induced detuning, is valid. We do this by performing numerical simulations to extract a value for the final intensity I_f and using Eq. 3.4 and Eq. 4.6 to extract values $\sigma_0 n$ that would be deduced from experimnet. We find that within the recoil time, both analytic expressions start to differ from the true atomic column density by over 5%, and the perturbative model of Eq. 4.6 quickly divereges thereafter.

In the following sections, we describe two versions of numerical simulations that we have performed in order to appropriately extract atomic column densities from experimental data.

4.3 Stationary atom model

In order to numerically simulate the imaging process, we assume a Gaussian distribution of atoms along the propagation direction, $\rho(z) = n/sqrt2\pi w e^{(-z^2/2w^2)}$. The dependence of the result on the choice of cloud width w is discussed in the next chapter. We divide the cloud into small bins along z. For the initial version of the simulation, the atoms were assumed to stay within the same bins for the entire duration of the imaging pulse, i.e. the cloud shape remained constant. We
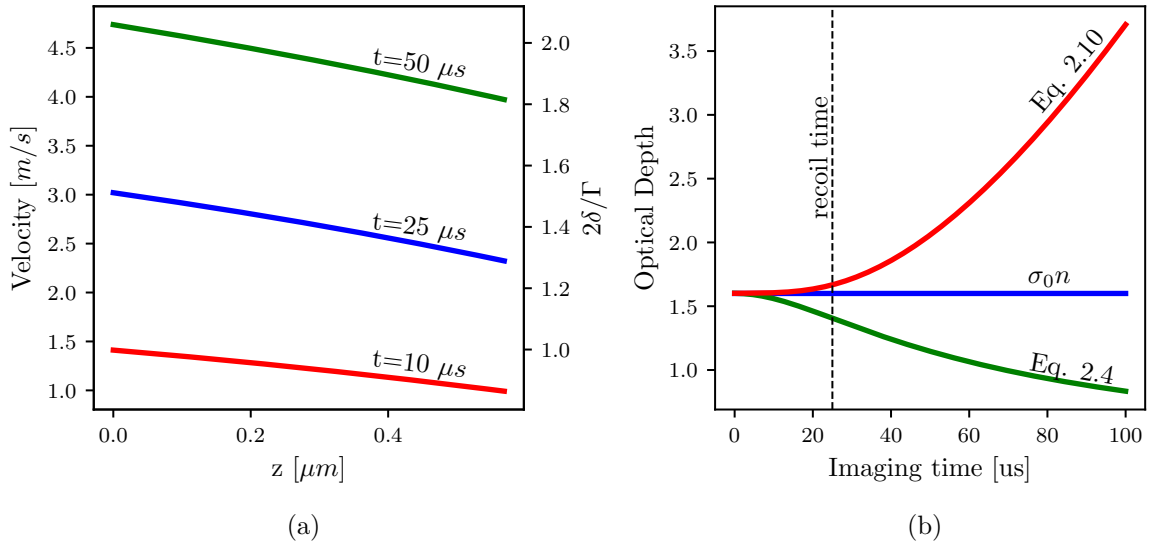
Figure 1: (a) Dependence of velocity and detuning on position simulated for ^{40}K at three different imaging times and a probe intensity $I_0 = 0.8 I_{\text{sat}}$. (b) Column densities deduced from optical depths obtained from recoil detuning corrected simulation of on-resonant imaging of ^{40}K atoms at probe intensity $I_0 = 0.8 I_{\text{sat}}$. The blue line is the input column density $\sigma_0 n = 1.6$. The green line is the high probe intensity corrected column density given by Eq. (3.4). The red line is the column density as expanded to second order in time, Eq. (4.6).

then used Eqs. 4.1-4.2 to numerically propagate the probe intensity and detuning as a function of both time and space. The algorithm used is detailed by Alg. 1.

Algorithm 1 Stationary atom model

$I[n = 0, t] = I_0$ {n is the bin index, t is the time index, I is in units of I_{sat}}
$\delta[n, t = 0] = 0$ {light initially resonant, δ in units of $\Gamma/2$}
$H_f = 0$ {Radiant fluence seen by camera after passing through cloud}
for $t = 0$ to t_f **do** {loop over time steps}
   for $n = 1$ to N **do** {loop over bins, N is total bin number}
      $A = \sigma_0 \rho[n] dz$ {dz is the size of spatial step}
      $B = v_r dt/(\hbar c \rho[n])$ {dt is the size of the time step}
      $I[n, t] = I[n - 1, t] - AI[n - 1, t]/(1 + \delta[n, t - 1]^2 + I[n - 1, t])$ {Eq. (4.1)}
      $\delta[n, t] = \delta[n, t - 1] + B\left(I[n - 1, t] - I[n, t]\right)$ {Eq. (4.2)}
   end for
   $H_f = H_f + I[N, t] dt$ {collecting total fluence seen by the camera}
end for
$OD^{\text{sim1}} = -\ln\left(H_f/I_0 t_f\right)$

We call the optical depth obtained in this way OD^{sim1}, to distinguish if from the simulated optical depth via the method described in the next section.

The validity of this model can be checked by considering limits where the equations are analytically solvable. For short imaging times, the recoil-induced detuning should not contribute to the optical depth, and therefore Eq. 3.4 should become exact. This is seen in Fig. 2a, where the imaging pulse is only 3 μs long and the simulated optical depth (blue dots) agrees with that given by Eq. 3.4 for all intensity regimes.

Even at longer imaging times, the problem can be analytically solved for limits of both high and low intensity compared to the saturation intensity. At intensities $I \gg I_{\text{sat}}$, even far detuned atoms will scatter light at their maximum, and we can assume $\delta^2/\Gamma^2 \ll I/I_{\text{sat}}$, reducing back to Eq. 3.4. At extremely low intensities, atoms will scatter very little light and the detuning $\delta^2/\Gamma^2 \ll 1$, again reducing back to Eq. 3.4. As seen in Fig. 2 b,c the simulation agrees with the analytic Eq. 3.4 in the limit of both high and low intensities. But, as the imaging time increases, the disagreement due to recoil induced detuning grows.
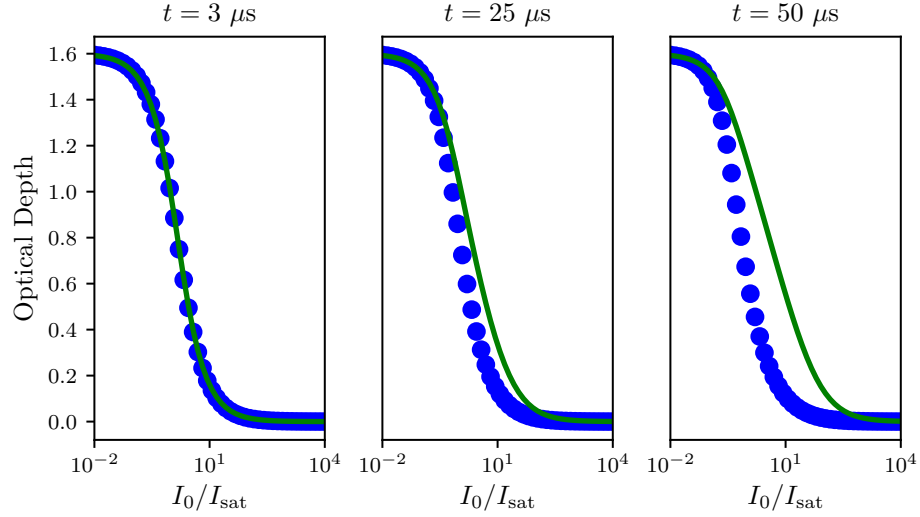
Figure 2: Optical depth as a function of probe intensity as predicted by the simulation (blue symbols) and by Eq. (3.4) (green curves), for three different imaging times. As expected, the predictions agree in both the high and low intensity limits, and differ for probe intensities comparable to the saturation intensity and longer imaging times.

The simulation allows us to extract both the intensity and the detuning as a function of both time and position. We can use this information to infer the velocity and therefore the displacement of the atoms during the imaging pulse, and check if our assumption that the atoms stay in their original 'bins' during the image pulse is valid. Figure 3a shows the position, deduced by integrating the recoil-induced velocity, as a function of time of the first, middle, and last spatial 'bin' for a probe intensity slightly above saturation, $I = 1.2 I_{\text{sat}}$. As seen in the figure, not only do the atoms move beyond their 'bins', but also at long imaging times the first atoms (which have absorbed the most light) overtake the last ones. Therefore, the atomic cloud does not maintain shape during the imaging pulse, and our initial assumption is invalid.

(a)

(b)
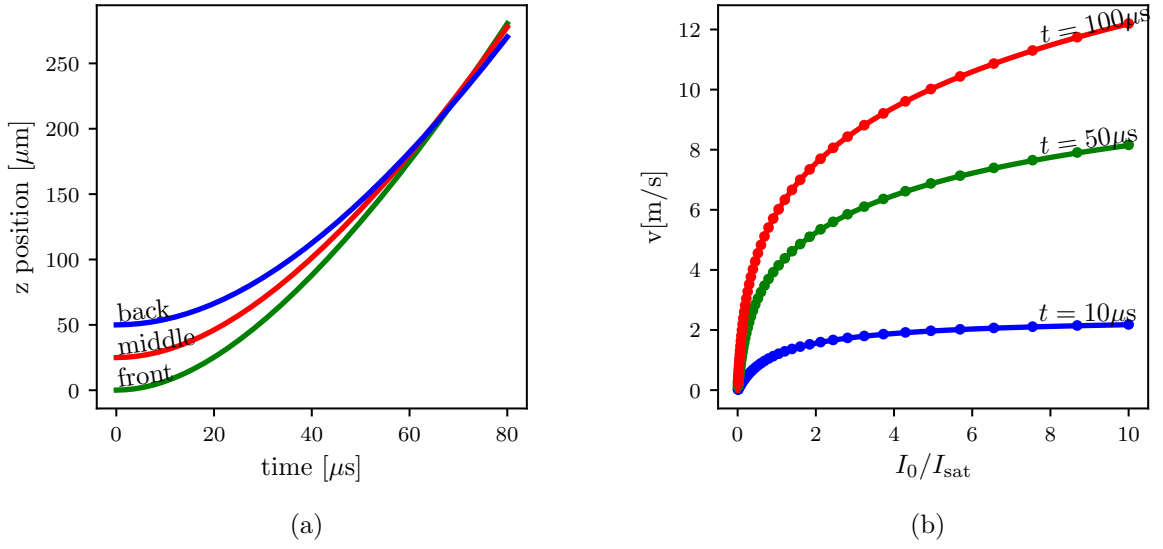
Figure 3: (a) Position of atoms as a function of imaging time for atoms in the first (solid green), middle (dashed red), and last (dotted blue) bins of the simulated density distribution for an initial cloud 50 μm in extent. The probe intensity used in this calculation was $1.2\,I_{\text{sat}}$, and the column density was $\sigma_0 n = 1.6$. (b) The velocity of a single composite atom as a function of probe intensity for various imaging times. Simulation data (dots) and numerical solutions of Eq. (4.7) (lines) are in agreement.

4.4 Traveling atom model

To model the recoil-induced detuning effect during the imaging pulse taking into account the potentially significant spatial displacement of the atoms, we performed a second version of our simulation. In this version, we clumped some number of atoms N_{ca} into a single composite atom, and then tracked the detuning, velocity and position of each composite atom as a function of imaging time. Tacking individual atoms would be computationally inaccessible for reasonable cloud sizes. The algorithm used is given by Alg. 2.

Algorithm 2 Travelling atom model

$z[n] = z_0$, $\delta[n] = 0$ {initialize position and detuning for each composite atom, labeled by index n}
$O[i] = n$ {make a list of composite atom indexes, ordered by position}
$I[n = 0, t] = I_0$ { t is the time index, I is in units of I_{sat}}
$H_f = 0$ {Radiant fluence seen by camera after passing through cloud}
for $t = 0$ to t_f **do** {loop over time steps}
  for $i = 1$ to N **do** {loop over superatoms}
    $n = O[i]$ {apply probe intensity to composite atoms in order of appearance}
    $A = \sigma_0 N_{sa} dz$ {dz is length over which atoms were grouped into single composite atom}
    $B = v_r dt/(\hbar c N_{sa})$ {dt is the time step}
    $I[n, t] = I[n - 1, t] - AI[n - 1, t]/(1 + \delta[n]^2 + I[n - 1, t])$ {Eq. (4.1)}
    $\delta[n] \mathrel{+}= B\left(I[n - 1, t] - I[n, t]\right)$ {Eq. (4.2), detuning in units of $\Gamma/2$}
    $z[n] \mathrel{+}= dt\Gamma\delta/2k$ {k is the wavenumber, $\Gamma\delta/2k$ is the velocity at δ detuning}
  end for
  $O[i]=\mathrm{sort}(n, \mathrm{key} = z[n])$ {sort composite atom indexes by current position}
  $H_f H_f + I[N, t]dt$ {collecting total fluence seen by the camera}
end for
$OD^{\mathrm{sim2}} = -\ln\left(H_f/I_0 t_f\right)$

To check the validity of this version of the simulation, we check the velocity of a composite atom as a function of time in an analytically solvable limit. In this case, we take the limit of a single composite atom, such that the intensity seen by the composite atom becomes time independent. This simplifies Eqs. 4.1 and 4.2 to only carry time dependence in the detuning term, and we can then plug Eq. 4.1

into Eq. 4.2 and differentiate both sides with respect to time to obtain

$$\frac{d\delta(t)}{dt} = \frac{\Gamma k_r v_r}{2} \frac{I/I_{\text{sat}}}{1 + 4\delta^2/\Gamma^2 + I/I_{\text{sat}}}. \tag{4.7}$$

Equation (4.7) can be solved numerically, and is in agreement with our simulation, as seen in Fig. 3(b).

We then used this version of the simulation to look at the motion of composite atoms as a function of imaging time in phase space (ie, velocity and position). Some examples of this motion can be seen in Fig. 4. As seen in the figure, the atomic cloud is significantly distorted during the imaging pulse and the atoms perform some crazy acrobatics.

It remains to check how the atoms' acrobatics affect the resulting optical depth, ie the attenuation of the probe beam. To do this, we compare the optical depths generated by our stationary atom model, OD^{sim1} , and by our travelling atom model, OD^{sim2}. The results of this comparison are seen in Fig. 5(a). As seen from the figure, the optical depths predicted by the two versions of the simulation are negligibly small - $\left| OD^{\text{sim1}} - OD^{\text{sim2}} \right| / OD^{\text{sim1}} \leq 0.005$. We also checked the effect of having different initial distributions of atoms in space by varying the initial function $\rho(z)$ and keeping the total atom number constat. We found the effect of this to be negligible as well. Therefore, to infer atomic column densities from observed optical depths, it is sufficient to use the satationary atom model.

4.5   Calibration of saturation intensity

Saturation intensity is an intrinsic propety of the atom, so the idea of calibrating it may be confusing. However, there are several experimental parameters that may influence exactly what value of I_{sat} is appropriate to use in Eq. 4.1 and 4.2, such as losses in the imaging system and polarization of the probe beam. In
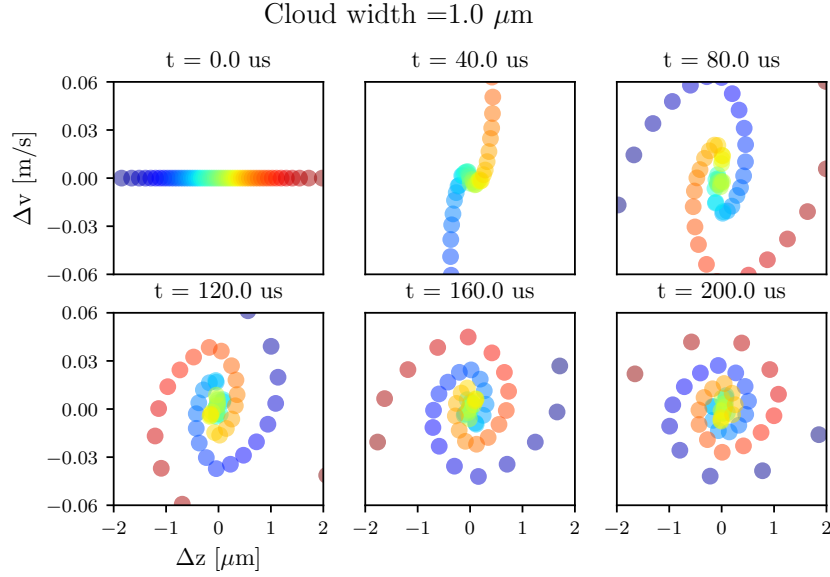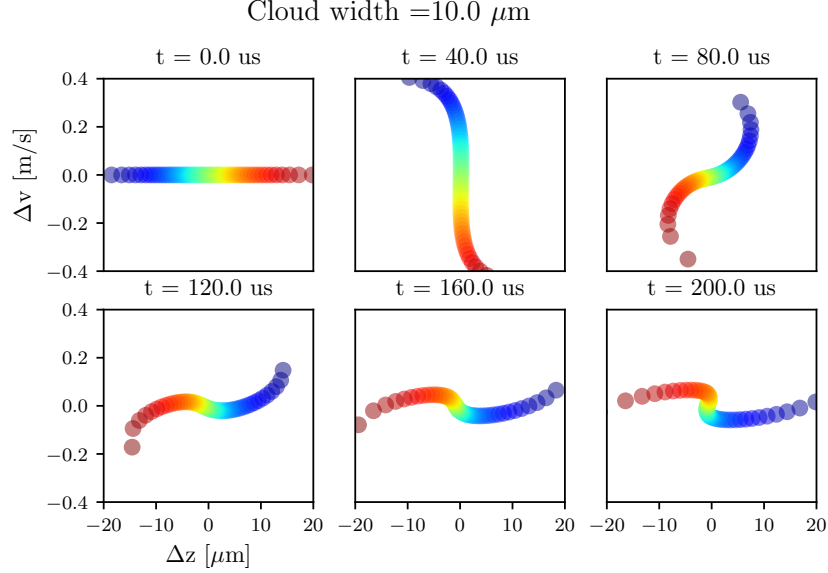
Figure 4: Phase space evolution of an atomic cloud exposed to probe light with intensity $\tilde{I}_0 = 1.2$. We defined $\Delta v = v - \langle v(t) \rangle$ and $\Delta z = z - \langle z(t) \rangle$, subtracting out the center of mass position and velocity of the cloud. The column density $\sigma_0 n$ is 1.6, and the initial cloud is a Gaussian with a width of 10 μm in (a) and 1 μm in (b). The center of mass velocities $\langle v \rangle$ are (0, 3.41, 5.26, 6.52, 7.50, 8.32) m/s sequentially, and are the same for both initial cloud widths.
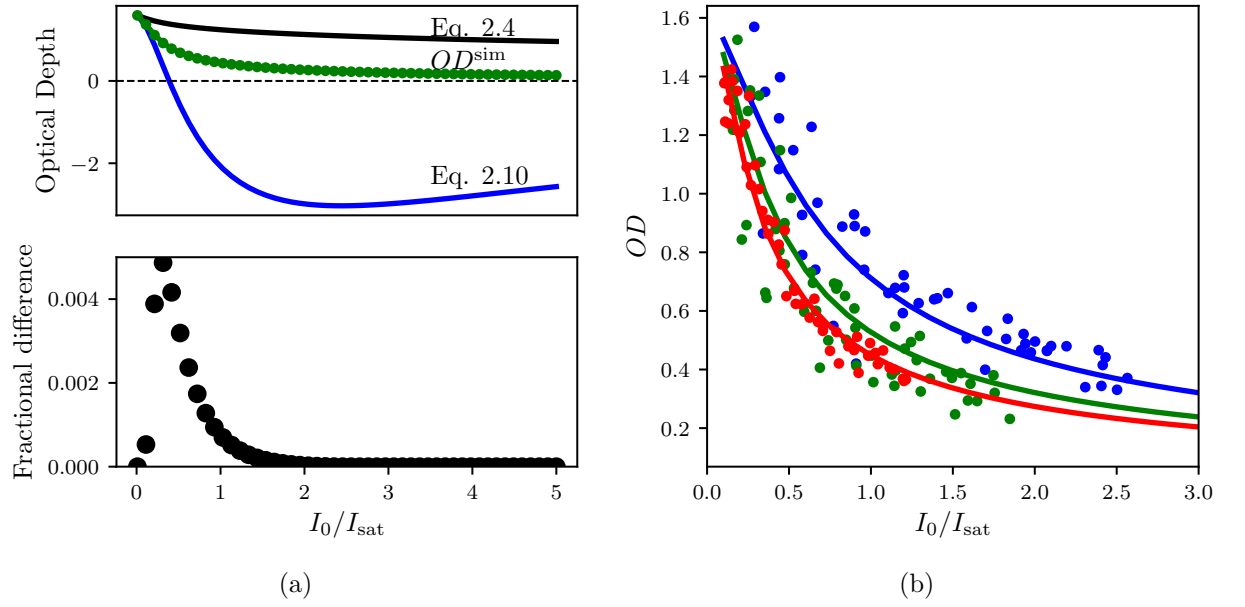
Figure 5: (a) Top. Optical depth as a function of probe intensity for an imaging time $t = 100$ μs. $OD^{(1)}$ and $OD^{(2)}$ are optical depths predicted from a given column density by Eq. (3.4) and (4.6) respectively. The two versions of simulated optical depth, OD^{sim1} (green curve) and OD^{sim2} (green dots) are plotted. Bottom. The fractional difference between two versions of the simulated OD, $\left|OD^{\text{sim1}} - OD^{\text{sim2}}\right|/OD^{\text{sim1}}$. (b) The optical depth as a function of probe intensity for three imaging times: $t = 40$ μs (cyan), $t = 75$ μs (magenta), $t = 100$ μs (red). The dots represent experimental data and the lines represent the best fit of simulated data. The optimal fit parameters pictured are a $\sigma_0 n$ of 1.627(5) and saturation intensity of 29(7) counts/μs.

addition, we have no direct experimental access to the total radiant fluence (time integral of intensity) seen by the camera. Instead, the light hitting the charge-coupled device (CCD) camera triggers some number of photoelectrons to be registered. The proportionality between the number of photons hitting the camera and the number of photoelectrons it triggers is called the quantum efficiency q_e of the camera. The number of these photelectrons, after some electronic gain and noise introduced during the readout process, is then read out as a number of 'counts' registered on each pixel. The camera-dependent factors influencing how the number of counts depends on the number of incoming photons can be convolved with the experimental factors of probe polarization and optical loss into a single calibration of the effective saturation intensity in units of 'counts' output by the camera per unit time.

To calibrate this effective I_sat in camera counts per unit time, we absorption imaged our cloud of ^{40}K atoms for a range of probe intensities for three different values of imaging time: 40 μs, 100 μs, and 200 μs. We select a small region in the center of the cloud, where we can assume the atomic column density $\sigma_0 n$, and the initial probe intensity I_0 to be roughly constant. We then average the values of I_0 and I_f over this region and plot the final intensity I_f as a function of I_0. We then used the optical depth predicted by our simulation OD^sim and used that to simultaniously fit the three curves with I_sat and $\sigma_0 n$ as fit parameters, as shown in Fig. 5(b). As can be seen from the figure, this procedure not only allows us to read off I_sat in units of camera counts per μs, but also shows that our simulation accurately reproduces the differences in OD dependenc on imaging time.

4.6   SNR optimization

Using the simulations described in the previous sections, we can create a lookup table of atomic column densities as a function of initial and final probe intensities I_0 and I_f for any given imaging time. This lookup table can be then used to interpret

experimental data and obtain the atom number in regimes where the recoil-induced detuning is significant. This procedure can also be used to propagate photon shot noise into uncertainty in measured atom number.

We consider Poisson distributed photon shot noise, converting into shot noise on photoelectrons triggered inside the CCD. The standard deviation will then be proportional to $q_\mathrm{e}\sqrt{N_p}$, where q_e is the quantum efficiency of the camera and N_p is the photon number. This uncertainty can be then propagated via the lookup table into uncertainty on the measured atomic column density $\delta_{\sigma_0 n}$. The signal-to-noise ratio (SNR) can then be expressed as $\sigma_0 n/\delta_{\sigma_0 n}$.

We study the SNR as a function of imaging time and initial probe intensity for a few different atomic column densities. Some representative data is shown in Fig. 6. As seen in Fig. 6(a), for a wide range of atomic column densities, extending the imaging time beyond 40 μs no longer yields significant improvements in SNR. There is, however, a factor of 1.5 improvement between using an imaging time of 10 μs, where the simple model given by Eq. 3.4 is appropriate, and 40 μs. Therefore, there are signifiant gains that can be made by going to longer imaging times and making use of the simulated lookup table.

This simulation allowed us to interpret experimental data. For a given imaging time, we created a look-up table of predicted optical depth as a function of probe intensity and atomic column density. We then found the observed optical depth on this table, with the given probe intensity, and inferred the atomic density. The uncertainty in the measured intensities can be propagated through this procedure, and we established optimal imaging parameters to maximize the SNR of this detection scheme. Figure 6(b) illustrates that the optimal initial probe intensity is different for different atom numbers. For low atom numbers, $\sigma_0 n \approx 0.1$, a probe intensity of $I_0 \approx 0.6 I_\mathrm{sat}$ is best.
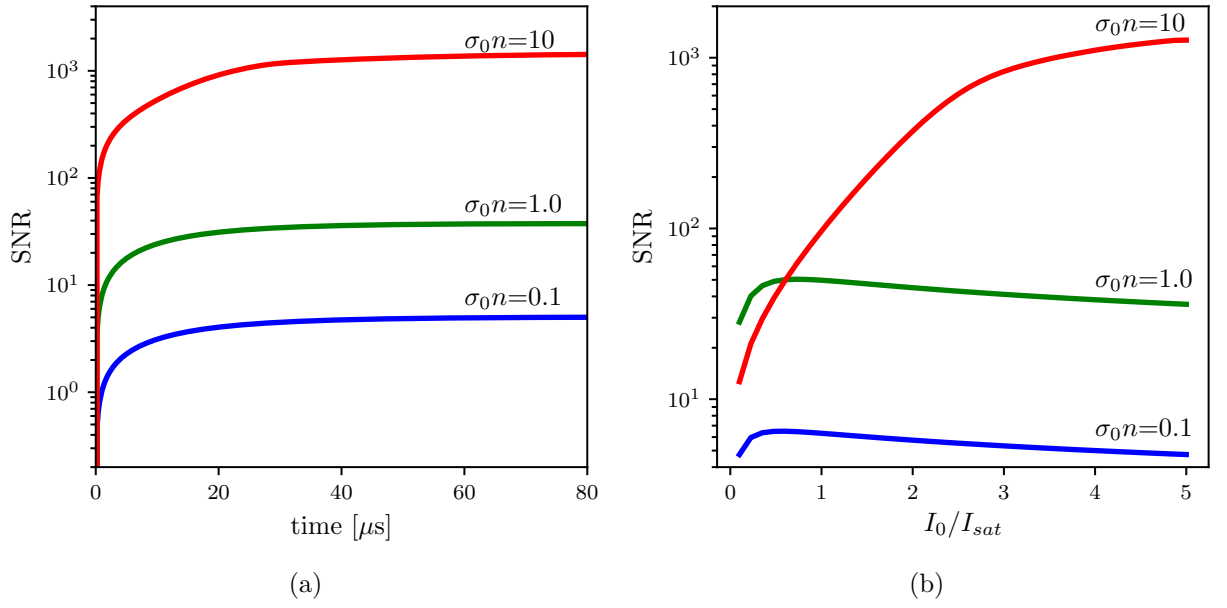
Figure 6: SNR for three different column densities after correcting for recoil induced detuning. (a) SNR as a function of imaging time for a probe intensity of $I_0 = 5.0 I_{\text{sat}}$ and (b) SNR as a function of probe intensity for an imaging time of 50 μs.

Chapter 5: Direct Imaging of Scattering Near a Feshbach Resonance

In this chapter, we describe our experiment directly imaging s-wave scattering halos of ^{40}K atoms in the vicinity of a Fesbach resonance between the $|F = 9/2, m_F = -9/2\rangle$ and $|F = 9/2, m_F = -7/2\rangle$ internal states. We used this data to extract the location of the magnetic fields resonance of 20.206(15) mT and a width of 1.0(5) mT, similar to the accepted values of 20.210(7) mT and 0.78(6) mT [11]. The data presented in this chapter was previously reported in [9].

We first introduced Feshbach resonances in section 2.2.2. Although Feshbach resonances are extremely useful for studying and manipulating Fermi gases, their resonant magnetic field values are difficult to predict analytically and are commonly computed via numerical models based on experimental input parameters [12–14] or determined experimentally [15, 16]. There have been a variety of experimental techniques used to characterize Feshbach resonances, including measuring atom loss due to three-body inelastic scattering, measurement of re-thermalization timescales, and anisotropic expansion of the cloud upon release from a confining potential, all of which infer the elastic scattering cross section from collective behavior of the cloud [17–19].

Here, we present an alternative technique, where we directly image the enhancement in elastic scattering due to the resonance. We collided pairs of ultra-cold Fermi gases and directly imaged the resulting s-wave scattered atoms as a function of magnetic field strength. This allowed us to observe the enhancement in scattering without relying on proxy effects. We measured the fraction of atoms scattered

during the collision, and from this fraction deduced the resonant magnetic field and the width of the resonance.

In our dilute DFGs, even with the resonant enhancement of the scattering cross section, only a small fraction of the atoms scattered as the clouds passed through each other. This made direct detection of scattered atoms difficult due to detection uncertainty that disproportionately affected regions of low atomic density. To optimize the signal-to-noise ratio (SNR) for low atom numbers, we absorption imaged with fairly long, high-intensity pulses — a non-standard regime, where the atoms acquired a velocity during imaging and the resulting Doppler-shift was non-negligible. Simulation of the absorption imaging process was necessary for an accurate interpretation of these images, as described in Chapter 4. Using the simulation-corrected images, we extracted the fraction of atoms scattered in our collision experiment.

5.1 Experimental procedure

We prepared our degenerate ^{40}K clouds as described in section 2.3.3.

We used adiabatic rapid passabe (ARP) to transfer the degenerate cloud of ^{40}K atoms in the $|F = 9/2, m_F = 9/2\rangle$ state into the $|F = 9/2, m_F = -9/2\rangle$ state by using a 3.3 MHz rf field and sweeping the bias magnetic field from -0.518 mT to -0.601 mT in 150 ms.

Following the state transfer, we had two versions of the protocol – one for approaching the Feshbach resonance from higher fields and one for approaching it from lower fields. For approaching the resonance from lower fields, we proceeded by ramping the bias magnetic field to 19.05 mT, turning on a 42.42 MHz RF field, and then sinusoidally modulating the bias field at 125 Hz for 0.5 s, with a 0.14 mT amplitude, decohering the ^{40}K state into an equal mixture of $|F = 9/2, m_F = -9/2\rangle$ and $|F = 9/2, m_F = -7/2\rangle$. For approaching the resonance from higher fields, the same was done at a bias field of 21.71 mT and an RF frequency of 112.3 MHz. The

depolarization allowed the [40]K atoms to interact and re-thermalize, allowing us to further evaporate in the dipole trap [20]. Since [87]Rb is heavier than [40]K, we were able to evaporate the [40]K atoms past the point where [87]Rb atoms were no longer suspended against gravity and had been completely removed. These hyperfine states of [40]K were then used to study their Feshbach resonance.

After evaporation, we ramped the bias field in a two-step fashion to the desired value B near the Feshbach resonance. We approached the field using our quad coils in Helmholtz configuration [PUT IN REFERENCE TO WHERE THEY ARE TALKED ABOUT IN THE INTRO CHAPTER](0.19 mT/A) to bring the magnetic field to a setpoint 0.59 mT away from B, $B - 0.59$ mT when approaching from below and $B + 0.59$ mT from above. We held the atoms at this field for 100 ms to allow the eddy currents induced by the large quad coils to settle, and then used our lower inductance biasZ coils PUT IN REFERENCE TO WHERE THEY ARE TALKED ABOUT IN THE INTRO CHAPTER[] (0.017 mT/A) set of Helmholtz coils to quickly change the field the remaining 0.59 mT. This allowed us to study the resonance from both sides without the added losses associated with going through the resonance [21].

Once at the intended bias field, we split the cloud into two spatially overlapping components with opposing momenta and observed scattering as they moved through each other and separated. These counterpropagating components were created using an $8E_\mathrm{L}$ deep near resonant (λ_L=766.704 nm) 1-d retro-reflected optical lattice [PUT IN REFERENCE TO WHERE IT IS TALKED ABOUT IN THE INTRO CHAPTER], where $E_\mathrm{L} = \hbar^2 k_\mathrm{L}^2/2m_\mathrm{K}$ is the lattice recoil energy and $\hbar k_\mathrm{L} = 2\pi\hbar/\lambda$ is the recoil momentum. We rapidly pulsed this lattice on and off with a double-pulse protocol [22, 23]. The pulse sequence was optimized to transfer most of the atoms into the $\pm 2\hbar k_\mathrm{L}$ momentum states. Since the initial Fermi gas had a wide momentum spread (in contrast to a BEC, which has a very narrow momentum spread),

and the lattice pulsing is a momentum dependent process [22], not all the atoms were transferred into the target momentum states. We experimentally optimized our pulse times to minimize the atoms remaining in the zero momentum state. The optimized pulse times were 23 μs for the first pulse, 13 μs off interval, and 12 μs for the second pulse [23].

We then released the atoms from the trap and allowed 1 ms for the two opposite momentum states within the cloud to pass through each other, scattering on the way. For the data taken coming from below the Feshbach resonance, we then simply ramped down the field and imaged the atoms. For the data taken coming from above the Feshbach resonance, we ramped the field back up, retreating through the resonance if it had been crossed and thereby dissociating any molecules that were created, and then quickly ramped the field back down and imaged the atoms. We used a 40 μs imaging pulse with $I_0/I_{\text{sat}} \approx 0.6$ at the center of the probe laser. The total time-of-flight was $t_{TOF} = 6.8$ ms.

The magnetic fields produced by the combination of our quad and biasZ coils in the regime of interest were independently calibrated by rf-spectroscopy. We prepared ^{40}K atoms in the $|F = 9/2, m_F = -9/2\rangle$ state and illuminated them with and rf-field with some frequency ν_{rf}. We then ramped our high-inductance coils to variable set points, followed by an adiabatic 250μs ramp of 2.84 mT in the lower inductance coils. We then used Stern-Gerlach and observed the fractional population in the $|F = 9/2, m_F = -9/2\rangle$ and $|F = 9/2, m_F = -7/2\rangle$ states as a function of the high-inductance coil current. We fit the fractional population curve to a Gaussian, and considered the center of the fit to be on-resonant, with an uncertainty given by the Gaussian width. We used the Breit-Rabi formula [ADD CITATION TO THIS ONCE ITS PUT INTO THE HYPERFINE SECTION OF ATOM LIGHT CHAPTER] to determine the resonant field value at ν_{rf}. We did this for 5 different rf frequencies, and acquired a field calibration with an uncertainty of 0.3 mT, which
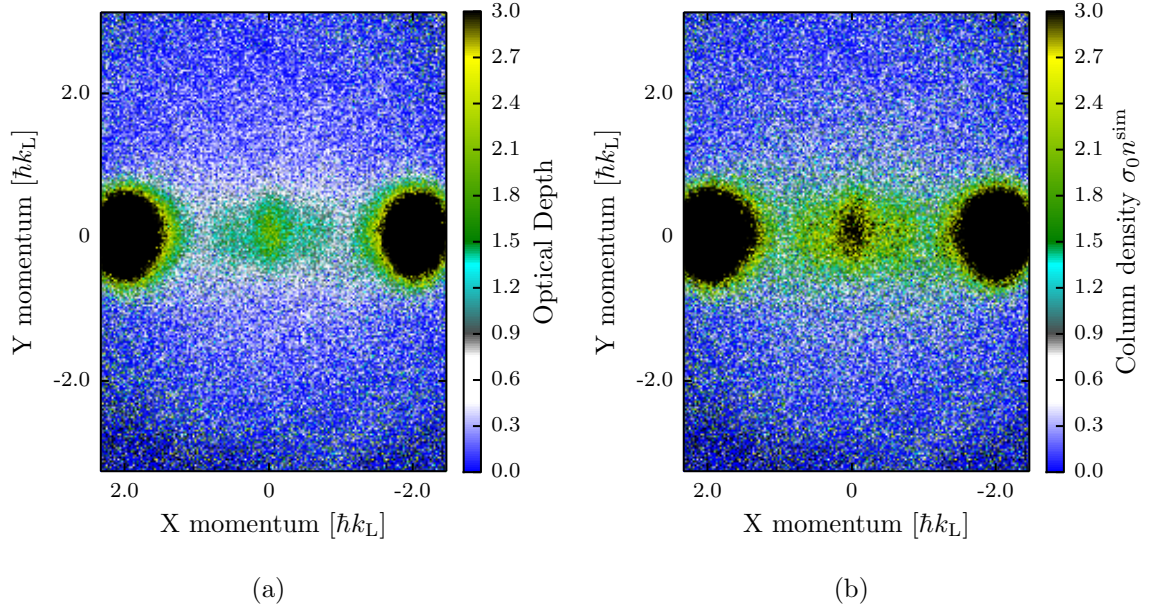
Figure 1: An example of our absorption image after 6.8 ms TOF. The 1-D lattice imparts momentum along $e_{\mathbf{x}}$. The two large clouds on the left and right are the atoms in the $\pm 2k_{\mathrm{L}}$ momentum orders that passed through each other unscattered. The smaller cloud in the center is the atoms that remained in the lowest band of the lattice after pulsing, and thus obtained no momentum. The thin spread of atoms around these clouds is the atoms that underwent scattering. This image was taken coming from below the Feshbach resonance at 20.07 mT. (a) Raw optical depth, (b) atomic column density obtained by comparing to simulated ODs, $\sigma_0 n^{\mathrm{sim}}$

was included in the listed uncertainty on the center field of the Feshbach resonance.

5.2   Data analysis

We first processed each image by comparing the obseved ODs to simulations taking into account the recoil induced detuning as described in Chapter 4. An example of images before and after processing are shown in Fig. 1. To improve the signal and mitigate our shot to shot number fluctuations, we took 15 nominally identical images for each data point.

We counted the fraction of atoms that experienced a single scattering event for each of the fifteen images at a given bias magnetic field. Single scattering events are easily identified, as two atoms that scatter elastically keep the same amplitude of
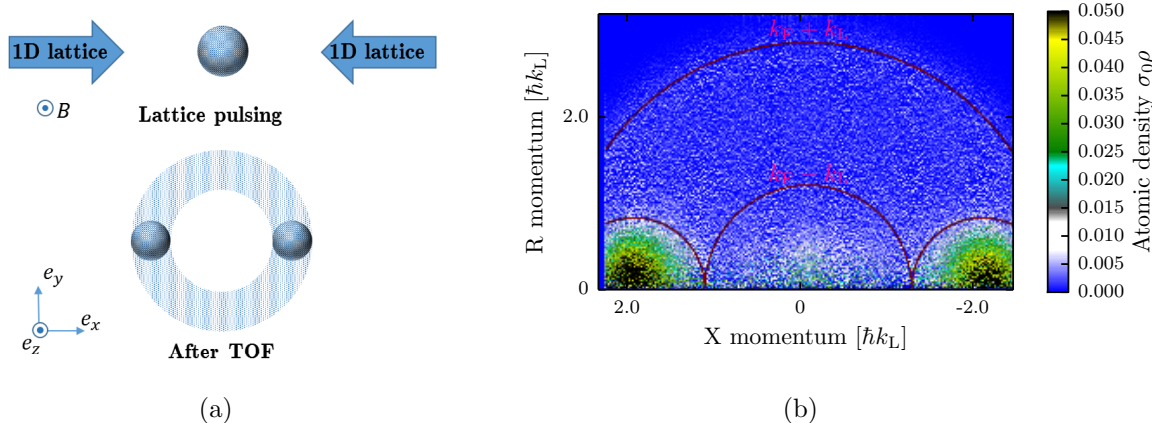
Figure 2: (a) Our experimental setup. After time-of-flight, the two clouds traveling along $\pm\hat{e}_x$ directions have separated and the atoms that underwent a single scattering event were evenly distributed in a scattering halo around the unscattered clouds. The 1-D lattice defined the axis of cylindrical symmetry. (b) Inverse Abel transformed image. The atoms within the Fermi momentum k_F of each unscattered cloud center are in the unscattered region and counted towards the total unscattered number. The atoms outside the radius $k_L - k_F$ but inside $k_L + k_F$ while also being outside the unscattered region are counted towards the number of single scattered atoms.

momentum, but depart along an arbitrary direction. Therefore, an atom traveling at $2\hbar k_L$ to the right that collides elastically with an atom traveling at $-2\hbar k_L$ to the left will depart with equal and opposite momenta $2\hbar k_L$ at an arbitrary angle, and in a time-of-flight image such atoms will lie in a spherical shell, producing the scattering halo pictured in Fig. 2(a).

Absorption images captured the integrated column density along e_z, a projected 2D atomic distribution. To extract the radial dependence of the 3D distribution from the 2D image, we performed a standard inverse Abel transform. The inverse Abel transform assumes cylindrical symmetry, which was present in our case, with the axis of symmetry along e_x, defined by the lattice. We neglect the initial asymmetry of the trap, as during time-of-flight the atoms travel far beyond the initial extent of the cloud $(r_x, r_y, r_z) \approx (45,48,15)$ μm, while the cloud width after TOF is ≈ 82 μm in each direction. We thus obtained the atomic distribution $\rho(r, \theta)$

as a function of r, the radial distance from the scattering center, and θ, the angle between r and symmetry axis $e_\mathbf{x}$, integrated over ϕ, the azimuthal angle around the x axis.

We then extracted the number of scattered atoms N_scat as a fraction of the total atom number N_tot for each image, as shown in Fig. 2(b). The unscattered atom number was the number of atoms in the two unscattered clouds. The number of atoms that underwent a single scattering event was the number of atoms outside the Fermi radius of the unscattered clouds, but inside the arc created by rotating the Fermi momentum k_F around the original center of the cloud (red arcs in Fig. 2(b)). For both the scattered and unscattered numbers, we accounted for atoms that fell outside the field of view of our camera by multiplying the counted atom number by a factor of the total area as defined by the radii divided by the visible area on the camera. The atoms in the center region were not counted as they were originally in the zero momentum state and could not contribute to the scattering halo under study.

We fit the fraction of scattered atoms versus the total atom number for each of the 15 images taken at the same bias magnetic field to a line constrained to be zero at zero. The slope of this fit was taken to be the value of $N_\text{scat}/N_\text{tot}^2$ at that bias magnetic field, and the variance of the fit gave the uncertainty on that data point. This uncertainty reflected our shot to shot number fluctuations, which produced variable atomic densities and thus influence the scattered fraction.

We then deduced the resonant field value B_0 and width of the resonance Δ, the parameters in Eq. (2.26). Since we were in the low energy regime (the atomic momentum was much smaller than the momentum set by the van der Waals length $k_\text{L} + k_\text{F} \ll 1/l_\text{vdW}$, and we were well below the p-wave threshold temperature [20]), the scattering cross-section was given by $\sigma = 4\pi a^2$.

The scattering cross-section σ gives the probability $P_\text{scat} = \sigma N/A$ that a single

particle will scatter when incident on a cloud of atoms with a surface density of N/A, where A is the cross-sectional area of the cloud and N is the number of atoms in the cloud. In our case, each half of the initial cloud, with atoms number $N_{\text{tot}}/2$, is incident on the other half. Thus, the number of expected scattering events is $N_{\text{scat}} = (N_{\text{tot}}/2)\sigma(N_{\text{tot}}/2) = \sigma N_{\text{tot}}^2/4A$. Assuming A is constant for all our data, we can define a fit parameter $b_0 = 4\pi a_{\text{bg}}^2/4A$, where a_{bg} is the background scattering length. We can thus adapt Eq. (2.26) to obtain the fit function

$$\frac{N_{\text{scat}}}{N_{\text{tot}}^2} = b_0 \left(1 - \frac{\Delta}{B - B_0}\right)^2 + C. \tag{5.1}$$

We found that our imaging noise skewed towards the positive, giving rise to a small background offset. We accounted for this in our fit by including a constant offset parameter C.

5.3 Results

Our final data is presented in Fig. 3. The red curve depicts a best fit of the model given in Eq. (5.1). The fit parameters we extracted were $\Delta = 1(5)$ mT, $B_0 = 20.206(15)$ mT, $b_0 = 5(3) \times 10^{-3}$ and $C = 8(1) \times 10^{-4}$. To obtain the fit, we used data taken by approaching the resonance from above for points above where we expected the resonance to be and data taken approaching the resonance from below for points below. We also excluded from the fit data points very near the resonance, as there the assumption $\sigma\rho \ll 1$, where ρ is the atom number per unit area, is no longer valid and the problem must be treated hydrodynamically.

The accepted values for the ^{40}K s-wave Feshbach resonance for the $|9/2, -9/2\rangle$ and $|9/2, -7/2\rangle$ states are $B_0 = 20.210(7)$ mT and $\Delta = 0.78(6)$ mT [11], which is in good agreement with our findings. Some potential sources of systematic uncertainty that we did not account for include scattering with atoms that did not receive a
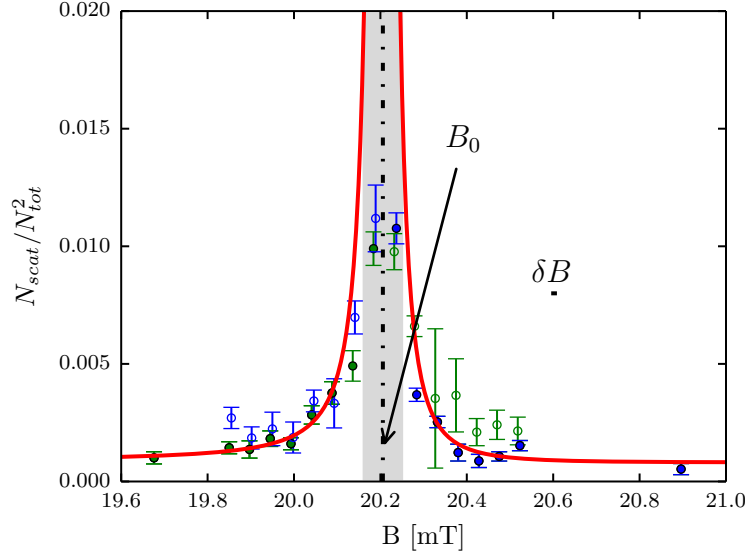
Figure 3: Normalized scattered population plotted versus bias field B. Green dots represent data taken coming from below the resonance, and blue dots represent the data taken coming from above the resonance. The red curve depicts the best fit, where data coming from above the resonance was used above the resonance and data coming from below the resonance was used below the resonance to create the fit; the unused data points are indicated by hollow dots. The regime where the scattering length is likely large enough for the atoms to behave hydrodynamically is shaded in gray, and data points in that area were also excluded from the fit. Resonant field value B_0 as found in this work and our systematic uncertainty in the bias magnetic field δB_0 are indicated.

momentum kick from the lattice pulsing or the impact of multiple scattering events.

Bibliography

[1] W. Ketterle and M. W. Zwierlein. Making, probing and understanding ultracold Fermi gases. In *Ultracold Fermi Gases, Proceedings of the International School of Physics 'Enrico Fermi', Course CLXIV*, Varenna, 20-30 June 2006.

[2] Daniel Adam Steck. Rubidium 87 d line data. Available online, http://steck.us/alkalidata, April 2018. revision 2.1.5.

[3] K. Jiménez-García, L. J. LeBlanc, R. A. Williams, M. C. Beeler, A. R. Perry, and I. B. Spielman. Peierls substitution in an engineered lattice potential. *Phys. Rev. Lett.*, 108:225303, May 2012.

[4] H.J. Metcalf and P. van der Straten. *Laser Cooling and Trapping*. Graduate Texts in Contemporary Physics. Springer New York, 1999.

[5] N.W. Ashcroft and N.D. Mermin. *Solid State Physics*. Saunders College, Philadelphia, 1976.

[6] Nicola Marzari, Arash A. Mostofi, Jonathan R. Yates, Ivo Souza, and David Vanderbilt. Maximally localized wannier functions: Theory and applications. *Rev. Mod. Phys.*, 84:1419–1475, Oct 2012.

[7] Karina Jimenez-Garcia. *Artificial Gauge Fields for Ultracold Neutral Atoms.* PhD thesis, Joint Quantum Institute, National Institute of Standards and Technology, and the University of Maryland, 2012.

[8] Daniel Adam Steck. Quantum and atom optics. Available online at http://steck.us/teaching, January 2015. revision 0.12.2.

[9] D. Genkina, L. M. Aycock, B. K. Stuhl, H-I Lu, R. A. Williams, and I. B. Spielman. Feshbach enhanced s-wave scattering of fermions: direct observation with optimized absorption imaging. *New Journal of Physics*, 18:013001, Dec 2015.

[10] Lindsey J. LeBlanc. *Exploring many-body physics with ultracold atoms.* PhD thesis, University of Toronto, 2011.

[11] C. A. Regal, M. Greiner, and D. S. Jin. Observation of resonance condensation of fermionic atom pairs. *Phys. Rev. Lett.*, 92(4), 2004.

[12] E. Tiesinga, B. J. Verhaar, and H. T. C. Stoof. Threshold and resonance phenomena in ultracold ground-state collisions. *Phys. Rev. A*, 47(5, B):4114–4122, 1993.

[13] M. Lysebo and L. Veseth. *Ab initio* calculation of Feshbach resonances in cold atomic collisions: *s*- and *p*-wave Feshbach resonances in $^6\text{Li}_2$. *Phys. Rev. A*, 79:062704, 2009.

[14] B. Gao. Analytic description of atomic interaction at ultracold temperatures. II. Scattering around a magnetic Feshbach resonance. *Phys. Rev. A*, 84:022706, 2011.

[15] S. Inouye, M. R. Andrews, J. Stenger, H. J. Miesner, D. M. Stamper-Kurn, and W. Ketterle. Observation of Feshbach resonances in a Bose-Einstein condensate. *Nature*, 392(6672):151–154, 1998.

[16] S. L. Cornish, N. R. Claussen, J. L. Roberts, E. A. Cornell, and C. E. Wieman. Stable Rb-85 Bose-Einstein condensates with widely tunable interactions. *Phys. Rev. Lett.*, 85(9):1795–1798, 2000.

[17] C. A. Regal and D. S. Jin. Measurement of positive and negative scattering lengths in a Fermi gas of atoms. *Phys. Rev. Lett.*, 90:230404, 2003.

[18] K. M. O'Hara, S. L. Hemmer, M. E. Gehm, S. R. Granade, and J. E. Thomas. Observation of a strongly interacting degenerate Fermi gas of atoms. *Science*, 298(5601):2179–2182, 2002.

[19] C. Monroe, E. Cornell, C. Sackett, C. Myatt, and C. Wieman. Measurement of Cs-Cs elastic scattering at $T = 30$ μK. *Phys. Rev. Lett.*, 70:414–417, 1993.

[20] B. DeMarco, J. L. Bohn, J. P. Burke, M. Holland, and D. S. Jin. Measurement of p-wave threshold law using evaporatively cooled fermionic atoms. *Phys. Rev. Lett.*, 82:4208–4211, 1999.

[21] C. Chin, R. Grimm, P. Julienne, and E. Tiesinga. Feshbach resonances in ultracold gases. *Rev. Mod. Phys.*, 82:1225–1286, 2010.

[22] S. Wu, Y.-J. Wang, Q. Diot, and M. Prentiss. Splitting matter waves using an optimized standing-wave light-pulse sequence. *Phys. Rev. A*, 71:043602, 2005.

[23] M. Edwards, B. Benton, J. Heward, and C. W. Clark. Momentum-space engineering of gaseous bose-einstein condensates. *Phys. Rev. A*, 82:063613, 2010.